TITLE

Heterogeneous substrate binding in a glutamate transporter homologue

AUTHORS

Krishna D. Reddy[1], Didar Ciftci[1,2], Amanda Scopelliti[1], Olga Boudker[1,3*]

AFFILIATIONS

[1] Department of Physiology and Biophysics, Weill Cornell Medicine, 1300 York Avenue, 10065, NY, USA

[2] Tri-Institutional Training Program in Chemical Biology, New York, NY 10064, USA

[3] Howard Hughes Medical Institute

* To whom correspondence should be addressed

ABSTRACT

Integral membrane glutamate transporters couple the concentrative substrate transport to ion gradients. There is a wealth of structural and mechanistic information about this family, including kinetic models of transport. Recent studies have revealed transport rate heterogeneity in an archaeal glutamate transporter homologue Glt_{Ph}, inconsistent with simple kinetic models. The structural and mechanistic determinants of this heterogeneity remain undefined. In a mutant form of Glt_{Ph}, we demonstrate substrate binding heterogeneity in the outward-facing state, modulated by temperature and salts. We observe similar trends in wild-type Glt_{Ph} that correlate with changes in the transport rate. Extensive cryo-EM analysis of the fully bound mutant Glt_{Ph} provides multiple potential explanations of heterogeneous substrate binding. At equilibrium, we show subtle differences in tilts of protomers in the outward-facing state and configurations of the substrate-binding pocket. Within seconds of substrate binding, we observe perturbed helical packing of the extracellular half of the substrate-binding domain. Some or all of these may contribute to the heterogeneity observed in binding and transport.

MAIN TEXT

Membrane glutamate transporters pump substrates against their concentration gradients, serving critical biological functions across all kingdoms of life. In mammals, excitatory amino acid transporters (EAATs) recycle glutamate from the synaptic cleft into the glia (Freidman et al., 2020). In prokaryotes, orthologous transporters uptake nutrients, with specific transporters taking up glutamate, aspartate, neutral amino acids, or dicarboxylic acids (Burguiere, Auger, Hullo, Danchin, & Martin-Verstraete, 2004; Kim et al., 2002; Youn, Jolkver, Kramer, Marin, & Wendisch, 2009). Transporters utilize energy from downhill ionic electrochemical gradients to carry concentrative substrate uptake. EAATs rely on inward Na^+ and proton gradients and an outward K^+ gradient (Zerangue & Kavanaugh, 1996). Prokaryotes utilize simpler mechanisms, where transport is coupled to either downhill proton or Na^+ gradients.

These transporters are homotrimers composed of a rigid scaffold domain responsible for trimerization, and a mobile transport domain containing the ligand-binding sites. Each protomer functions independently of the other two protomers (Erkens, Hanelt, Goudsmits, Slotboom, & van Oijen, 2013; Georgieva, Borbat, Ginter, Freed, & Boudker, 2013; Grewer et al., 2005; Koch, Brown, & Larsson, 2007; Koch & Larsson, 2005; Riederer et al., 2018; Ruan et al., 2017). Transport domains translocate ligands across membranes by moving ~15 Å from the outward-facing state (OFS) to the inward-facing state (IFS), termed an 'elevator' motion (Arkhipova, Guskov, & Slotboom, 2020; Garaeva, Guskov, Slotboom, & Paulino, 2019; Qiu, Matthies, Fortea, Yu, & Boudker, 2020; Reyes, Ginter, & Boudker, 2009). Several structural and mechanistic studies in prokaryotic Na^+-coupled transporters Glt_{Ph} and Glt_{Tk} have led to a simple kinetic model of transport (Alleva et al., 2020; Arkhipova et al., 2020; Boudker, Ryan, Yernool, Shimamoto, & Gouaux, 2007; Guskov, Jensen, Faustino, Marrink, & Slotboom, 2016; Oh & Boudker, 2018; Reyes, Oh, & Boudker, 2013; Riederer & Valiyaveetil, 2019; Verdon, Oh, Serio, & Boudker, 2014; X. Wang & Boudker, 2020). Briefly, in the OFS, ion binding to Na1 and Na3 sites reveals the substrate- and an additional sodium (Na2) binding site through an opening of helical hairpin 2 (HP2), which also prevents the translocation of Na^+-only bound transport domain. Subsequent binding of the substrate and Na2 closes HP2, allowing translocation to the IFS and ligand release into the cytoplasm.

Recently, high-speed atomic force microscopy, single-molecule Förster resonance energy transfer (smFRET) total internal reflection fluorescence (TIRF) microscopy, and ^{19}F-NMR revealed a more complex picture of Glt_{Ph} transport and dynamics (Akyuz, Altman, Blanchard, & Boudker, 2013; Akyuz et al., 2015; Ciftci et al., 2020; Erkens et al., 2013; Huang et al., 2020; Huysmans, Ciftci, Wang, Blanchard, & Boudker, 2021; Matin, Heath, Huysmans, Boudker, & Scheuring, 2020). These studies established the existence of additional conformational states in OFS and IFS, of which some translocate and transport at different rates. Though it is expected that cryo-EM studies would resolve these proposed conformational sub-states from heterogeneous datasets, this so far does not appear to be

the case (Arkhipova et al., 2020; X. Wang & Boudker, 2020). Therefore, the structural and mechanistic determinants of kinetic heterogeneity remain unclear. Using a mutant of Glt_{Ph}, we show that substrate binding in the OFS is also heterogeneous, consistent with at least two populations with different affinities. The populations can be modulated by salt and temperature, suggesting a conformational equilibrium between the substrate-binding states. The heterogeneous binding alone cannot explain the heterogeneous transport kinetics, but we show that it might be contributing. Based on an extensive analysis of the cryo-EM imaging data, we propose that a fraction of the transport domains in the absence of aspartate is in a more dynamic conformational state. We hypothesize that this state is the low-affinity binding state, favored by chaotropic anions and increased temperature.

RESULTS

P-Glt_{Ph} (S279E/D405N) reveals two outward-facing substrate-binding conformations modulated by temperature and salts

We generated a mutant, P-Glt_{Ph}, that eliminates Na^+ binding to Na1 (D405N) and introduces a protonatable residue at the tip of HP1 (S279E), mimicking amino acid sequence features of proton-coupled orthologues (**Figure 1** - **Supplementary Figure 1a**). We found that P-Glt_{Ph} has Na^+-dependent transport, greatly diminished compared to the WT transporter (Ryan, Compton, & Mindell, 2009). Proton gradients stimulated P-Glt_{Ph} activity in the presence of Na^+ (**Figure 1 - Supplementary Figure 1b**), though this is not the central focus of this study. Unexpectedly, P-Glt_{Ph} yielded a bimodal substrate-binding isotherm in isothermal titration calorimetry (ITC) experiments in the presence of 500 mM NaCl at 15°C (**Figure 1a-c**). Several binding models for complex equilibria, including cooperative and sequential binding models, cannot fit our data; furthermore, lack of coupling between protomers has been well-established (Erkens et al., 2013; Georgieva et al., 2013; Riederer et al., 2018; Ruan et al., 2017). A model assuming two independent, non-identical binding states (S1 and S2), referred to as a 'two-state' model from here on (Freire, Schon, & Velazquez-Campoy, 2009), is the simplest binding model that fits this data reliably. Thus, there are likely two dominant binding states, though there could be additional underlying complexity. The sums of the apparent stoichiometries (n_1 and n_2 values) averaged 0.97 ± 0.26 (range of 0.74-1.53, N=6) (**Figure 2 - Supplementary Tables 1 and 2**). Therefore, the two-state model likely represents two different conformations of the same site in the transporter population rather than two distinct binding sites within a protomer. The observed bimodal isotherms can be interpreted as having a conformation with a relatively higher affinity and lower exothermic enthalpy (S1) and a conformation with a relatively lower affinity and higher exothermic enthalpy (S2) (Brautigam, 2015; Le, Buscaglia, Chaires, & Lewis, 2013). Due to the lack of data points at the slope of the curve, we cannot accurately quantitate binding affinities of the states in ITC; however, the affinities of both S1 and S2 are in the nanomolar range. The two conformations must interconvert only slowly, or not at all, during the ITC experiment to manifest two distinct binding states. Notably, we do not observe bimodal isotherms in 50 mM NaCl, perhaps because the lower substrate affinity at lower Na^+ concentrations (Boudker et al., 2007; Reyes et al., 2013) blurs the distinctions between the states.

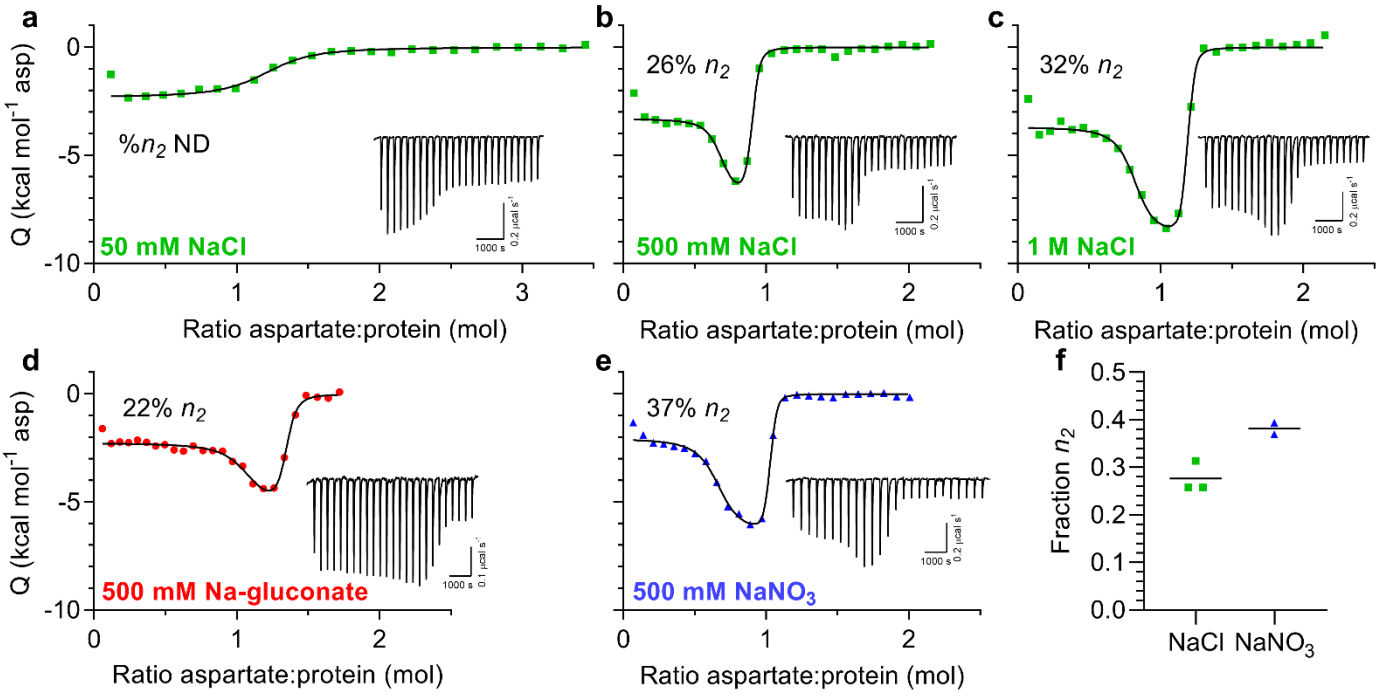

Figure 1. Heterogeneous substrate binding in P-Glt$_{Ph}$ (S279E/D405N). Shown ITC experiments were performed at 15°C. Insets show the thermal power with the corresponding scales. (a-c) Aspartate binding isotherms derived from the ITC experiments in the presence of different amounts of NaCl (green squares): 50 mM (a); 500 mM (b); and 1 M (c). The 50 mM data were fitted to the single-state model, with fitted K_d = 917 nM, ΔH = -2.3 kcal mol^{-1}, and an apparent number of binding sites, n = 1.18. 500 mM NaCl and 1 M NaCl data were fitted to the two-state binding model. The 500 mM NaCl data gave the following fitted parameters for the two states: K_d: 1.3 and 60.8 nM, ΔH: -3.3 and -7.1 kcal mol^{-1}, n: 0.64 and 0.22. The 1M NaCl data: K_d: 0.5 and 27.4 nM, ΔH: -3.7 and -8.7 kcal mol^{-1}, n: 0.77 and 0.38. (d-e) Aspartate binding isotherms obtained in 500 mM Na-gluconate (d, red circles), or $NaNO_3$ (e, blue triangles). All data were fitted to the two-state model. The 500 mM Na-gluconate data: K_d: 4.4 and 138.3 nM, ΔH: -2.3 and -5.5 kcal mol^{-1}, n: 1.00 and 0.28. The 500 mM $NaNO_3$ data: K_d: 0.9 and 34.3 nM, ΔH: -2.1 and -6.5 kcal mol^{-1}, n: 0.62 and 0.37. Experiments in (a-e) were performed at least twice on independently prepared protein samples with similar results. (f) Comparison of the n_2 fraction in 500 mM NaCl or $NaNO_3$. Each point is an independent experiment.

Increasing NaCl concentration from 500 mM to 1 M led to qualitative differences in the biphasic isotherms, attributed to increases in the S2 fraction and its exothermic enthalpy (**Figure 1b-c)**. The range of measured Na^+ K_D-s for WT Glt$_{Ph}$ is 99-170 mM (Hanelt, Jensen, Wunnicke, & Slotboom, 2015; Reyes et al., 2013; Riederer & Valiyaveetil, 2019), suggesting that Na1 and Na3 sites are already occupied at 500 mM NaCl. Thus, the S2 population might not depend on specific Na^+ binding and instead reflect general salting effects. To test this, we determined the S2 fraction in the presence of 500 mM sodium salts containing anions on different ends of the Hofmeister lyotropic series ($gluconate^-$ < Cl^- < NO_3^-) (Zhang & Cremer, 2006). Gluconate and nitrate have the opposite effects on protein structure; respectively, they decrease and increase the solubility of nonpolar molecules by increasing and decreasing bulk water structure - “salting out” and “salting in” effects. The biphasic shape of the binding isotherms is less pronounced in gluconate than nitrate, and chloride is an intermediate between the two (**Figure 1b, d-e**). Fitted binding parameters also demonstrate an increase in S2 fraction in $NaNO_3$ to ~38% at 15°C (**Figure 1f**). While our data suggest a decreased S2 fraction in Na^+-gluconate, the binding parameters were difficult to model reproducibly between replicates.

Decreasing temperature to 10°C resulted in the S2 fraction falling from 28±3% to 20±3% in 500 mM NaCl (**Figure 2 - Supplementary Tables 1 and 2**). At both 10 and 15°C, the two-state model fits the data with a larger than 5-fold difference in binding affinities between S1 (high-affinity) and S2 (low-

affinity) states and over 3.5 kcal mol^{-1} difference in binding enthalpies. Thus, we conclude that temperature and chaotropic anions modulate the relative population of S2, suggesting that S1 and S2 states are in equilibrium. We calculated the free energy differences between S1 and S2 before and after substrate binding based on the population differences and binding free energies measured at 10 and 15°C (**Figure 2a**). S1 and S2 are nearly isoenergetic before substrate binding, but S2 is much less favored when bound to L-Asp, reflecting lower affinity. Nevertheless, it must be kinetically stable over the course of ITC titrations.

To test where S1 and S2 may correspond to OFS and IFS, we measured single-molecule FRET (smFRET) signals using TIRF microscopy from fluorescently labeled P-Glt$_{Ph}$ solubilized in DDM. We introduced a single cysteine mutation into a cysteine-free background (P-Glt$_{Ph}$ C321A/N378C), labeled with donor and acceptor fluorophores, and analyzed by smFRET as in earlier studies (Akyuz et al., 2013; Akyuz et al., 2015; Huysmans et al., 2021). Conformations of protomer pairs within individual Glt$_{Ph}$ trimers can be distinguished by FRET efficiency (E_{FRET}) as either both in OFS (~0.4), a mixture of OFS and IFS (~0.6), or both in IFS (~0.8). Most P-Glt$_{Ph}$ molecules occupy a state showing low E_{FRET} associated with OFS in the presence of 500 mM sodium salts, regardless of anion or presence of substrate (**Figure 2b**). Therefore, we conclude that the high- and low-affinity conformations observed in ITC are both outward-facing.

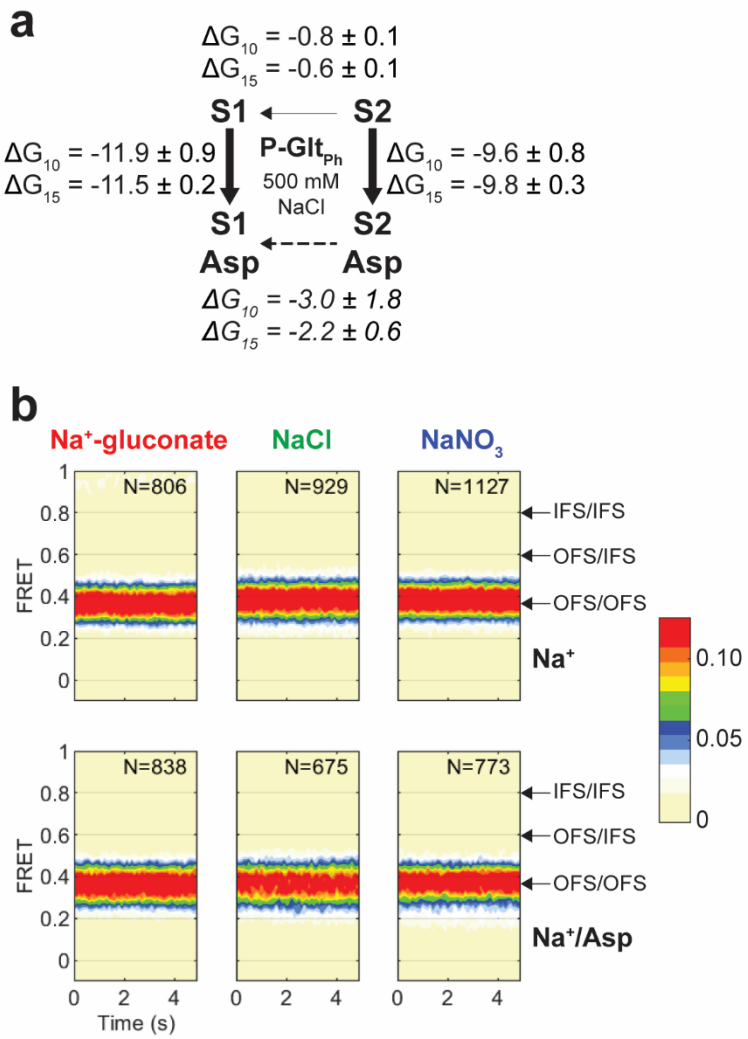

Figure 2. Heterogeneous substrate binding in P-Glt$_{Ph}$ occurs in the outward-facing state. (a) Schematic representations of the conformational and binding equilibria obtained experimentally at 10°C and 15°C (solid lines) or inferred (dashed lines). This was determined under the assumptions that there are only two states, and there is little to no interchange between substrate-free protein between injections of substrate. Directions of the arrows indicate directions of the free energy changes, ΔG-s, shown. All values are in kcal mol^{-1}. Binding ΔG-s are from Figure 2, Supplementary Tables 1 and 2. The free energy differences between sodium-bound outward-facing states were calculated from equilibrium constants $K_{eq}=n_1/n_2$. Thin lines represent steps that are slow on the time scale of ITC experiments. (b) FRET efficiency population histograms of P-Glt$_{Ph}$ in the presence of 500 mM salts (columns, indicated above the panels), either in the absence (top row) or presence (bottom row) of 1 mM L-Asp. *N* is the number of molecules analyzed. Data shown are aggregate two independent experiments. Population contour plots are color-coded from tan (lowest population) to red (highest). Expected conformations according to E_{FRET} values are indicated by arrows.

Heterogeneous substrate binding in wild-type Glt$_{Ph}$

We also performed ITC experiments on the WT protein to test for heterogeneous binding. Previously, we did not detect the presence of two binding states in Glt$_{Ph}$ conformationally constrained by cross-linking in OFS or IFS in saturating NaCl concentrations (Reyes et al., 2013). However, when we used

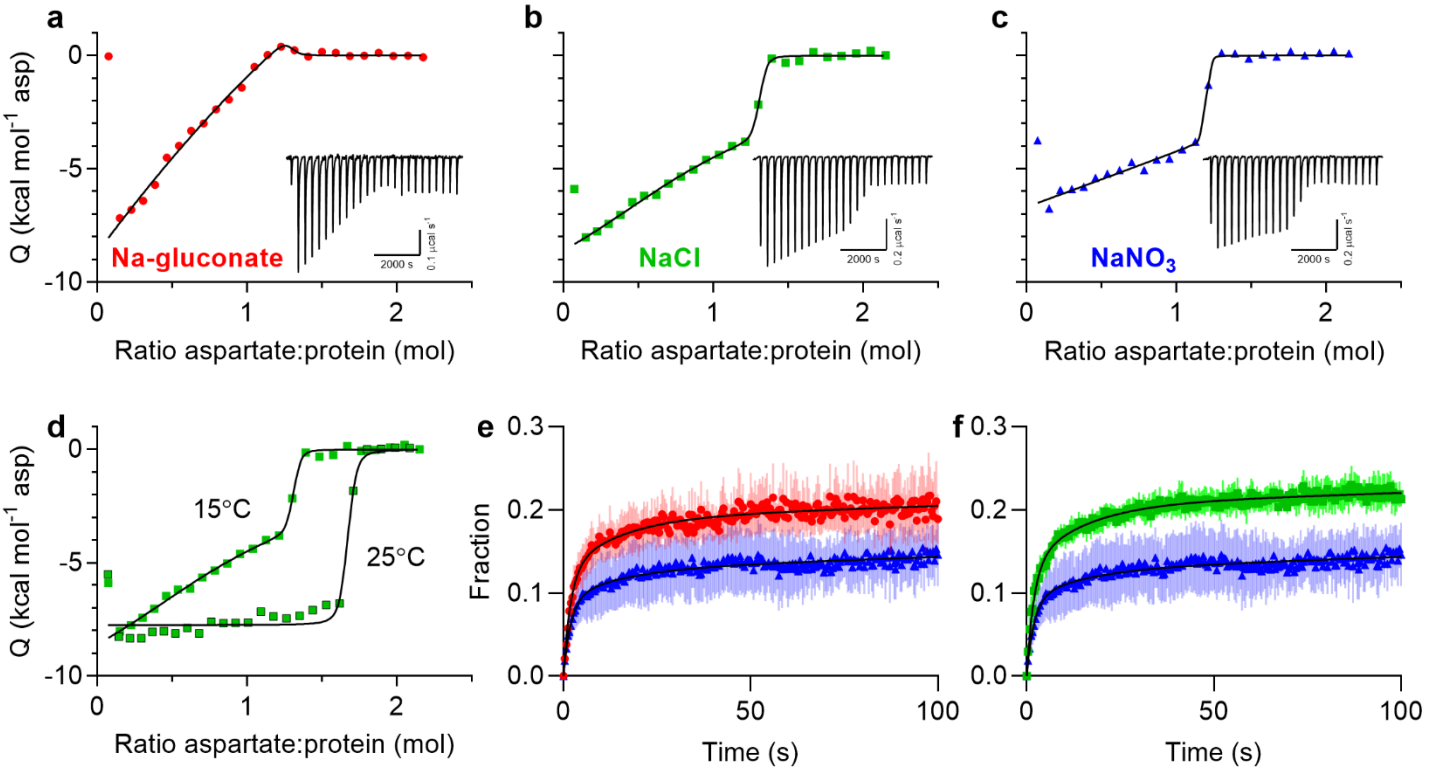

Figure 3. Heterogeneous substrate binding in WT Glt_{Ph}. Aspartate binding isotherms derived from the ITC experiments performed at 15°C in the presence of 500 mM (a) Na-gluconate (red circles); (b) NaCl (green squares); or (c) $NaNO_3$ (blue triangles). All data were fitted to the two-state model (black lines); however, the binding parameters are not reproducible. Insets show the thermal power with the corresponding scales. (d) Aspartate binding isotherms in 500 mM NaCl at 15°C (green squares) or 25°C (bordered green squares). The 25°C data was fitted to the independent binding model with a K_d of 8.1 nM, ΔH = -7.7 kcal mol^{-1}, and an apparent number of binding sites, n = 1.6. All experiments in (a-d) were performed at least twice on independently prepared protein samples, producing similar results. (e-f) Transport of Glt_{Ph} (C321A/N378C) measured using single-transporter FRET-based assay in $NaNO_3$ vs. Na-gluconate (e); or NaCl (f). Transport was initiated by perfusing surface-immobilized proteo-liposomes with buffer containing 200 mM sodium salt, 1 µM valinomycin, and 1 µM L-Asp. Data are shown as fractions of total observable transport over time, fitted to tri-exponential functions (black lines). The fitted parameters are in Figure 3 – Supplementary Table 1. Data are means and SE from three independent experiments.

unconstrained WT Glt_{Ph} at 15°C at high protein concentration to increase experiment sensitivity, we observed unusual features in aspartate binding isotherms (**Figure 3a-c**). Specifically, the initial L-Asp injections do not have constant heats as would be expected for a high-affinity single-site binding process. Instead, injection heats steadily decrease until the abrupt drop observed when the ligand saturates the protein. Here, the two-state model fits data better than the single-site model; however, the binding parameters (K_D, ΔH, or n) are not unambiguously modeled. Like in P-Glt_{Ph}, we observed qualitative differences in the isotherms obtained in different anions (**Figure 3a-c**) and temperatures (**Figure 3d**), suggesting a temperature- and salt-modulated equilibrium between binding states. Notably, the binding isotherm at 25°C looks nearly compatible with a single-site binding model (**Figure 3d**).

WT transporter in the presence of saturating Na^+ concentrations is predominantly in the OFS (Akyuz et al., 2013; Akyuz et al., 2015), but we cannot exclude that inward-facing protomers contribute to heterogeneous L-Asp binding. Thus, we also tested the binding of the transport blocker TFB-TBOA, which has a 100-fold preference for OFS (Boudker et al., 2007; McIlwain, Vandenberg, & Ryan, 2016; X. Wang & Boudker, 2020). We obtained bimodal ITC isotherms, though we could not quantify differences, if any, between TFB-TBOA binding in the presence of different anions (**Figure 3 – Supplementary Figure 1a-c**). When Glt_{Ph} saturated with TFB-TBOA was competed with L-Asp, we again observed bimodal isotherms. Thus, TFB-TBOA also binds to multiple conformations in OFS, and conformational heterogeneity persists after inhibitor binding (**Figure 3 – Supplementary Figure 1d-f**).

We used a recently developed smFRET-based single-transporter assay to see if anion-modulated populations of substrate binding states correlate with transport rates (Ciftci et al., 2020). Here, a fluorescently-labeled periplasmic glutamate/aspartate binding protein (PEB1a) reports on aspartate uptake. In this assay, P-Glt_{Ph} C321A/N378C mutant is labeled with PEG_{11}-biotin and N-ethyl maleimide (NEM) and reconstituted into liposomes; low protein-to-lipid ratios enrich vesicles containing at most one Glt_{Ph} trimer. These proteoliposomes are then loaded with PEB1a Y198F/N73C/K149C mutant with reduced amino acid affinity labeled with maleimide-activated donor (LD555P) and acceptor (LD655) fluorophores (referred to altogether as ccPEB1a-Y198F). The reconstituted, loaded proteoliposomes are immobilized in microscope chambers via biotinylated transporter and assayed for transport upon perfusion of saturating Na^+ and L-Asp concentrations. An increase in mean E_{FRET} from ~0.6 to ~0.8 reflects saturation of the ccPEB1a-Y198F sensor by L-Asp molecules transported into vesicles. This assay previously established kinetic heterogeneity in WT Glt_{Ph} transport (Ciftci et al., 2020), where at least three observable subpopulations ("fast," "intermediate," and "slow") transport at vastly different rates and all contribute to mean uptake measured in bulk. Most WT transporters are "slow," with turnover times of tens to hundreds of seconds.

Because Glt_{Ph} mediates an uncoupled anion conductance, which dissipates the buildup of membrane potential due to electrogenic transport, it shows faster uptake in the presence of more permeant anions ($gluconate^- < Cl^- < NO_3^-$) (Ryan & Mindell, 2007). Thus, we measured transport in K^+-loaded proteoliposomes in the presence of ionophore valinomycin clamping the potential. Upon perfusion of saturating amounts of external Na^+ and L-Asp, tri-exponential fits suggest that most molecules are in the "slow" transporting subpopulation regardless of anion, as expected. The fractions of the "slow" transporters were similar in Na-gluconate (81.1 ± 3.1) and NaCl (79.5 ± 3.4 %) conditions but increased in $NaNO_3$ conditions (87.3 ± 2.2 %) (**Figure 3e-f and Figure 3 – Supplementary Table 1**). Therefore NO_3^--favored low-affinity S2 conformation might correlate with a slower transporter population. However, experimental limitations prevent us from quantitatively comparing the conformational heterogeneity observed in ITC and single-transporter uptake assays.

High-resolution structures of P-Glt_{Ph} reveal subtle structural heterogeneity

Previously, crystallography and cryo-EM visualized an intermediate-outward facing state (iOFS), where the transport domain shifts partially inward (Arkhipova et al., 2020; Huang et al., 2020; Verdon & Boudker, 2012). The presence of iOFS or another previously unobserved outward-facing conformation could explain binding site heterogeneity in the OFS. We used cryo-EM to explore the conformational ensemble of outward-facing P-Glt_{Ph}. We first imaged P-Glt_{Ph} purified in the presence of 250 mM $NaNO_3$ and 1mM L-Asp (Dataset A). We froze grids from 25°C, which in the presence of $NaNO_3$ should increase the fraction of the S2 state, based on the ITC analysis. To maximally retain heterogeneity, we used a data processing approach designed to pick the highest-quality particles regardless of conformation (Su et al., 2020). We refined the maps to 2.2 Å after imposing C3 symmetry (**Figure 4 – Supplementary Table 1; Figure 4 – Supplementary Figure 2**). We observed several water densities within the transport domain contributing to the hydrogen bond network between substrate- and ion-coordinating residues. Interestingly, all six resolved buried water molecules are in the cytoplasmic half of the transport domain, "below" the substrate-binding site. In contrast, the extracellular half of the domain, "above" the substrate, appears "dry" (**Figure 4a**). The D405N mutation has previously been shown to abolish Na^+ binding at Na1 (Boudker et al., 2007); in its place, we observe an excess density suggesting that a water molecule replaces the ion (**Figure 4b**). The S279E side chain points into the extracellular milieu, away from the transport domain (**Figure 4c**).

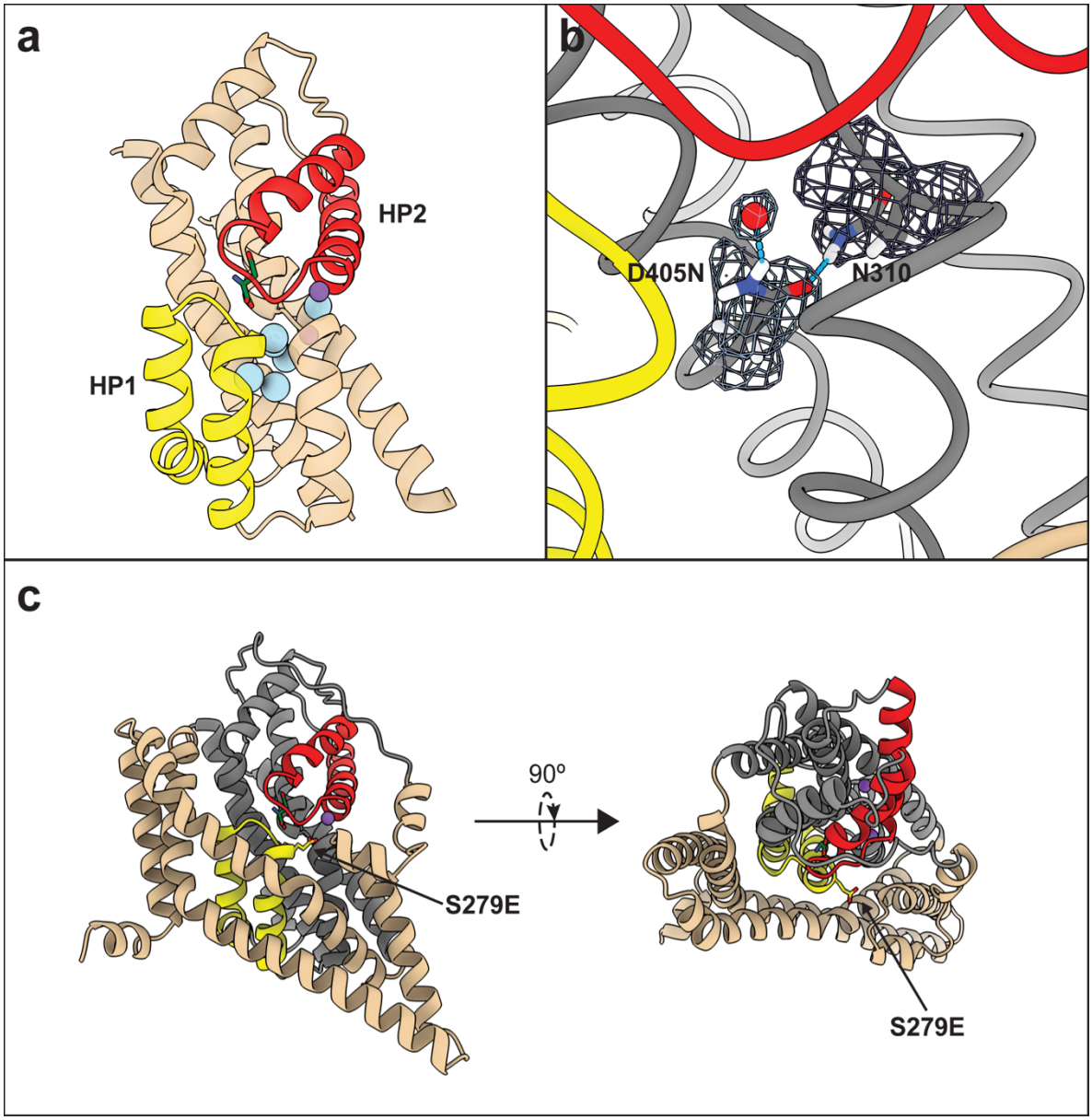

Figure 4. High-resolution structure of P-Glt$_{Ph}$. All images obtained from PDB ID 7RCP. (a) Cartoon representation of the transport domain with resolved waters shown as blue spheres. Sodium ions are purple spheres, the substrate is green, HP1 is yellow, HP2 is red. (b) Water molecule replacing Na1 and coordinated by D405N. Hydrogen bonds are displayed using 'hbond' in ChimeraX. (c) Cartoon representation of a protomer viewed in the membrane plane and from the extracellular space, showing S279E points away from the transport domain.

To find clues to the structural basis of substrate-binding heterogeneity, we searched for distinct P-Glt$_{Ph}$ conformations likely to exchange slowly on the ITC time scale. We used symmetry expansion followed by focused 3D classification around a single protomer, sorting ~1.6 million particles. This processing approach previously revealed the OFS and iOFS in the WT Glt$_{Ph}$ ensemble (Huang et al., 2020). However, all P-Glt$_{Ph}$ protomers resembled OFS (**Figure 5 – Supplementary Figure 1**), consistent with our smFRET data. We then locally refined each structural class on the entire trimer to 2.36-2.65 Å. When we superimposed protomers on trimerization regions of all three chains (residues 150-195), we observed three subtly different protomer tilts relative to the rest of the trimer, consisting of movements of the transport domain and parts of the scaffold not involved in trimerization (OFS$_{out}$, OFS$_{mid}$, and OFS$_{in}$) (**Figure 5 – Movie 1**). The largest tilt difference of 2.1° is between OFS$_{out}$ and OFS$_{in}$ transport domains. The tilt differences for OFS$_{out}$/OFS$_{mid}$ and OFS$_{mid}$/OFS$_{in}$ were ~1.1° each **(Figure 5a-c).** However, tilt axes were different for OFS$_{out}$/OFS$_{mid}$ and OFS$_{mid}$/OFS$_{in}$, and the three tilts do not occur along the same linear movement vector. The adjacent protomers are unaffected, suggesting that the movements occur independently in individual protomers (**Figure 5 – Movie 1; Figure 5 –**

Supplementary Figure 2). All classes are similar to the OFS crystal structure (PDB access code 2NWX, **Figure 5 – Supplementary Table 1**).

We also performed 3D Variability (3DVA) analysis on single protomers using the symmetry expanded particle stack, an unbiased way of observing components of continuous movements in cryo-EM data (Punjani & Fleet, 2021). We found movements comparable to those from OFS_{out} to OFS_{mid} and from OFS_{mid} to OFS_{in} in multiple variability components (**Figure 5 – Movies 2 and 3**), although the extent of tilts varied slightly between 3DVA maps and structures determined through focused classification.

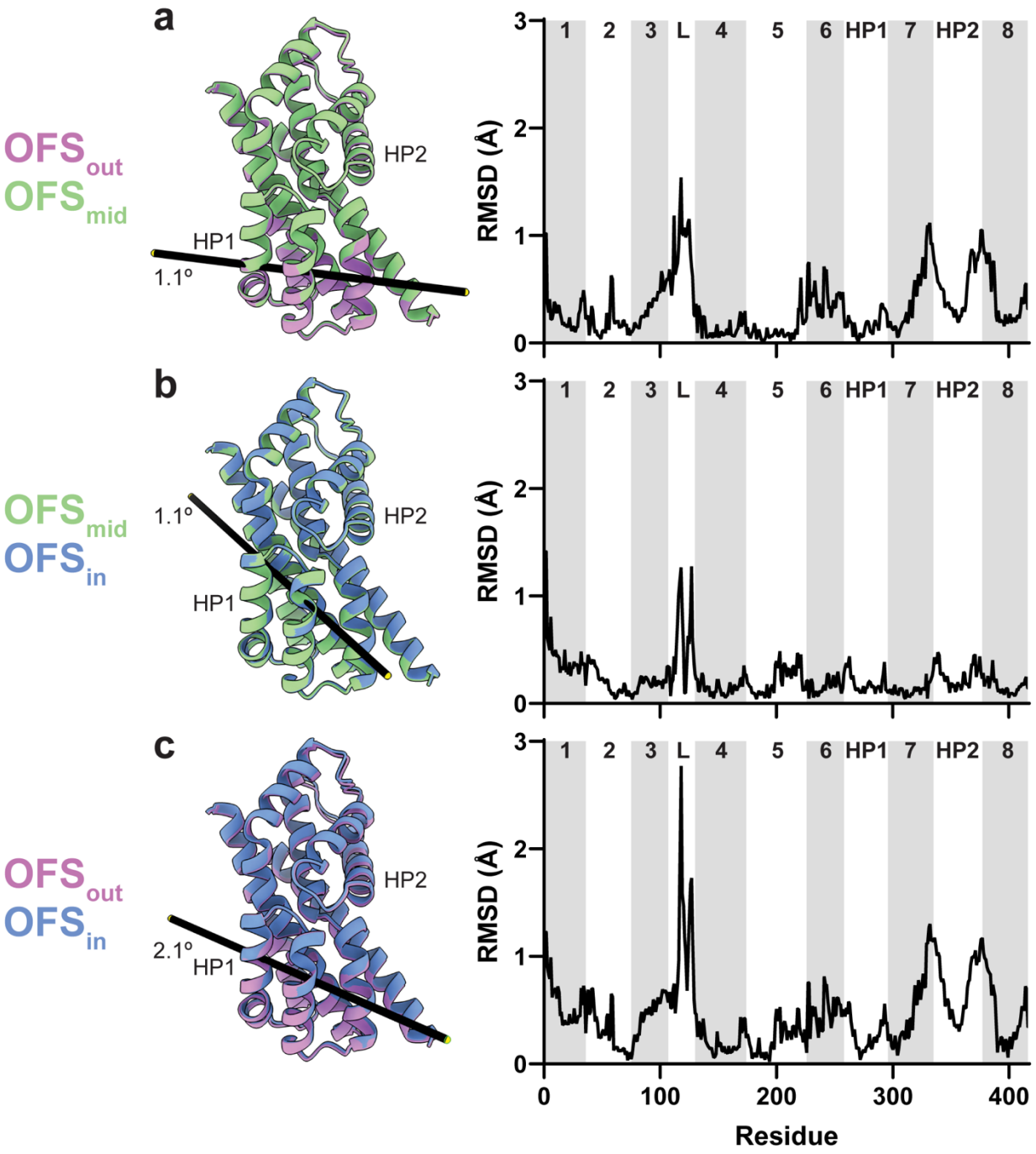

Figure 5. Protomer tilts in the outward-facing state. Trimers were superimposed on the trimerization regions (residues 150-195) of all three protomers. Comparison of the tilts for (a) OFS_{out}/OFS_{mid}; (b) OFS_{mid}/OFS_{in}; and (c) OFS_{out}/OFS_{in}. OFS_{out}, OFS_{mid}, and OFS_{in} are purple, green, and blue, respectively. Though parts of the scaffold domain also move (see Figure 5 – Movie 1), only transport domains of the classified protomers are shown for clarity. Black bars represent tilt axes and angles calculated using the 'align' command in ChimeraX. The corresponding per-residue Cα RMSDs are on the right. Transmembrane domains are labeled and alternatively shaded. 'L' denotes the flexible loop between TMs 3 and 4.

The high resolution of the data allowed us to examine the details of the substrate-binding sites. The sites of different structural classes were similar, except Asp-390 sampled unusual rotameric states in OFS_{out} conformations. Asp-390 is a highly conserved residue in TM8, which does not directly coordinate the substrate but is critical for the high-affinity L-Asp binding – D390A mutant has a 1000-fold higher dissociation constant (Riederer & Valiyaveetil, 2019). Arg-397 in TM8 is a principal substrate-coordinating residue. Its guanidinium group forms hydrogen bonds with the L-Asp sidechain carboxylate below (toward the cytoplasm) and cation-π interactions with Tyr-317 in TM7 above (toward the extracellular space). Asp-390 can be in a "down" rotamer, where it hydrogen-bonds to Arg-397, or an "up" rotamer, where it hydrogen-bonds to Tyr-317 (**Fig. 6a-b**). Our classification also revealed an intermediate rotamer between "down" and "up," which may represent an average of the two rotamers or a unique configuration (**Figure 6 – Supplementary Table 1**). These differences do not result in an observable change of the conformational state of Arg-397. However, interestingly, the engagement of tyrosine in hydrogen bonding through the OH group potentiates cation-π interactions compared to phenylalanine (Gallivan & Dougherty, 1999), and Y317F mutation leads to a 10-fold loss of L-Asp affinity in Glt_{Ph} (Riederer & Valiyaveetil, 2019).

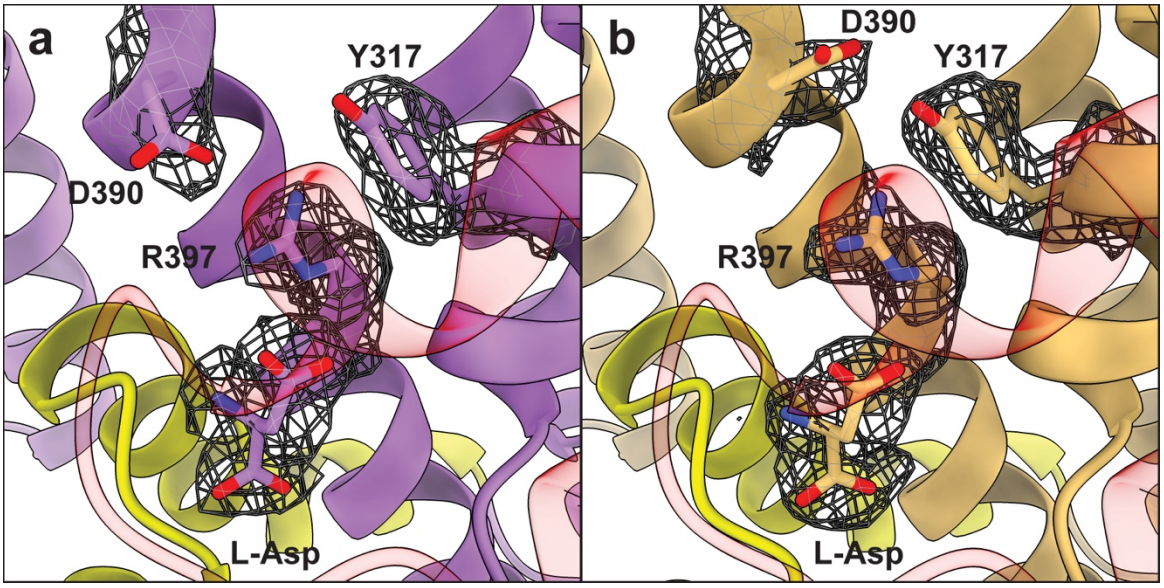

Figure 6: Two rotameric states of D390. Cartoon representations of OFS_{out} classes with "down" (a) and "up" (b) D390 rotamers. The mesh objects are density maps contoured at 4 σ; only densities within 1.5 Å of labeled residues are displayed for clarity. HP1 is in yellow, and HP2 in red.

Thus, the "up" and "down" rotamers might alter substrate affinity through different hydrogen bond patterns and local electrostatics. After further sorting out classes with ambiguous D390 densities, we found that only subpopulations of OFS_{out} classes, comprising ~10% of all particles, featured "up" or "intermediate" rotamers, while all OFS_{in} and OFS_{mid} classes showed either "down" rotamers or unresolved sidechain density (**Figure 6 – Supplementary Table 1; Figure 6 – Supplementary Figure 1**). Thus, the preference of Asp-390 to hydrogen-bond with Arg-397 or Tyr-317 may be allosterically coupled to the position of the transport domain. This might be significant because rotamer differences alone are unlikely to explain slowly switching substrate-binding states because sidechain rotations occur on a nanosecond time scale. If the rotameric preference is coupled to the transport domain tilt, then it is possible that the affinity state switches slowly. However, whether changes of the domain tilts are slow is also unclear, and we could not determine which inter- or intra-domain interactions are altered to produce different tilts.

Transient transport domain rearrangements in time-resolved cryo-EM

Our binding data suggests transiency of the low-affinity state after substrate binding, where the high-affinity state predominates at equilibrium. Thus, we collected a dataset where we pre-equilibrated

substrate-free P-Glt_{Ph} in 250 mM $NaNO_3$ and added 1mM L-Asp ~5 s before freezing from 25 °C (Dataset B). When we refined particles with C3 symmetry imposed, we obtained density maps with an overall resolution of 3.0 Å (**Figure 7 – Supplementary Figure 1**). The lower resolution compared to Dataset A may reflect increased structural heterogeneity but can also be due to different microscopes, imaging parameters, or artifacts of grid freezing.

After symmetry expansion and focused classification of single protomers followed by local refinement, we again observed all protomers in the OFS. We refined maps for four structural classes, ranging in resolution from 3.15 to 3.85 Å (**Figure 7 – Supplementary Figures 1 and 2; Figure 7 – Supplementary Table 1**). Class 3, which produced the highest-resolution map, structurally resembled the equilibrated P-Glt_{Ph} OFS_{mid} (RMSD of 0.293). Other classes showed a mixture of tilt states (**Figure 7 – Supplementary Table 2**). When we superimposed isolated transport domains on the intracellular regions (HP1, TM8b, and TM7a), "below" the substrate-binding site, we observed that they aligned well in structures from both datasets (**Figure 7a-b**). In contrast, we observed displacements of helices in the extracellular halves in Dataset B structures, around and "above" the substrate-binding site, most noticeable in HP2, TM8a, and TM7b (**Figure 7b**). We refrain from a detailed interpretation of side chains because of the moderate resolution of the maps. Nevertheless, these structural observations suggest that immediately upon substrate binding, a fraction of the transporter protomers experience a continuum of states. Because we observe minimal changes in these regions in pre-equilibrated dataset A (**Figure 7a**), we reason that the transport domain mobility may relax to a less heterogeneous state over time. Similar analysis of transport domains from the substrate-, inhibitor-, and Na^+-only bound Glt_{Ph} crystal structures (Alleva et al., 2020; Boudker et al., 2007) also reveal changes in TM7b and TM8a in addition to the expected changes in HP2, further supporting conformational lability of these regions (**Figure 7c**). Potentially, the ensemble of these states could manifest different substrate affinities.

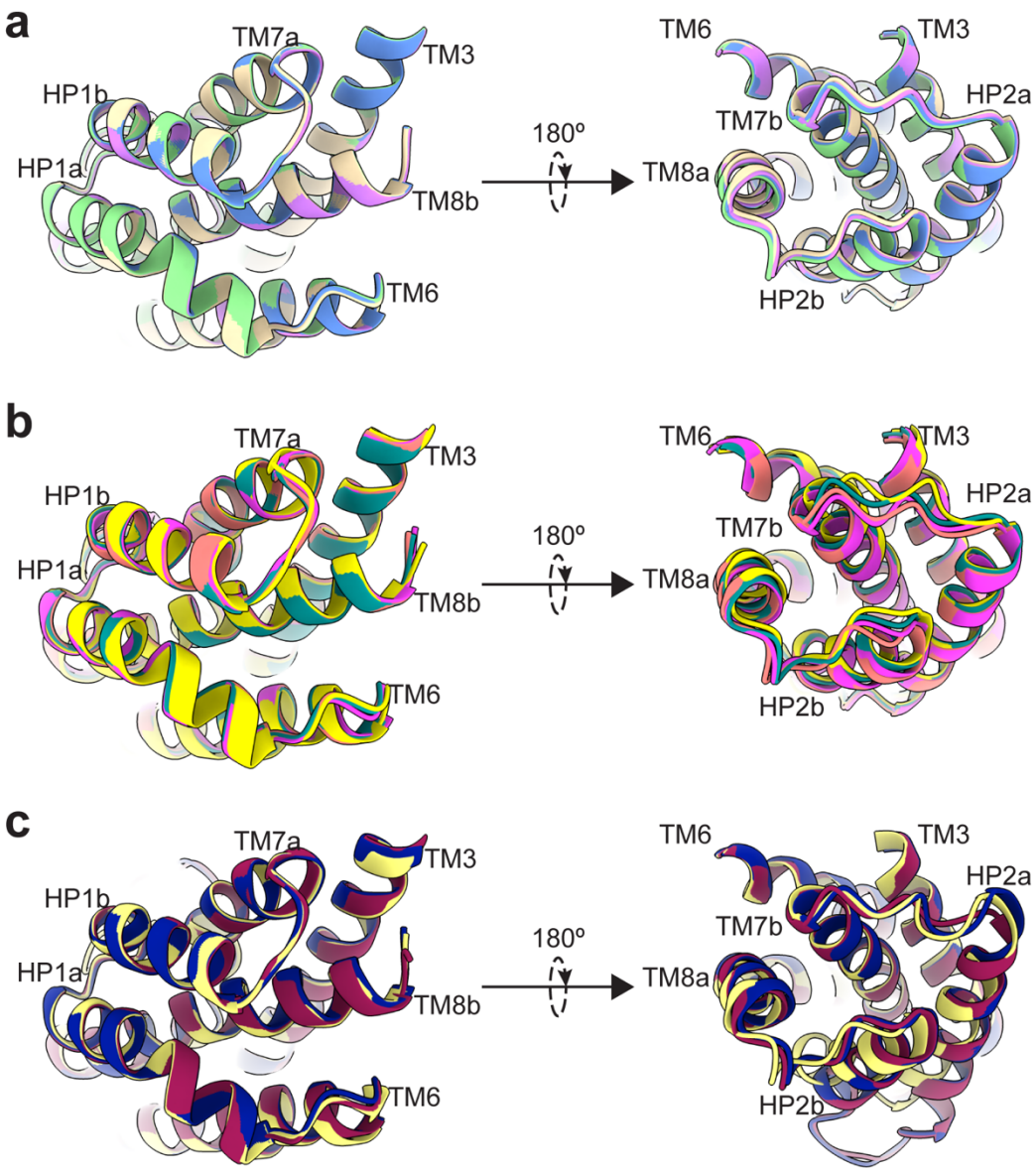

Figure 7. Mobility of transport domains helices. Transport domains were superimposed on HP1 and TM7a (residues 258-309). Superimposition of transport domains from Dataset A (a) and B (b). In (a), OFS_{out} (D390 down) is purple, OFS_{out} (D390 up) wheat, OFS_{mid} green, and OFS_{in} blue. In (B), B1 is salmon, B3 teal, B6 yellow, and B7 magenta. (c) Superimposition of crystal structures of substrate-bound (2NWX; light yellow), TBOA-bound (2NWW; dark blue), and Na^+-bound (7AHK; maroon) Glt_{Ph}. The views are from the intracellular (left) and extracellular (right) sides of the transport domain.

DISCUSSION

Serendipitously, we found that P-Glt_{Ph} mutant has two apparent substrate-binding states that seem to correspond to exchanging conformations because temperature and salts modulate their ratios (**Figure 1**). The states must exchange only very slowly and have sufficiently different affinities and enthalpies to manifest as two distinct binding sites in ITC (Brautigam, 2015; Le et al., 2013). WT isotherms lack the bimodal character of P-Glt_{Ph} but qualitatively suggests that WT follows the same rules, where salt chaotropicity and temperature alter the isotherm shapes by shifting the balance between the binding states (**Figure 3**). smFRET and cryo-EM revealed that P-Glt_{Ph} is predominantly outward-facing (**Figure 2**), possibly due to S279E mutation at the tip of HP1. In contrast, WT protein samples more states, including iOFS and IFS, which may also contribute to the binding equilibrium leading to isotherms lacking clear bimodal character (Akyuz et al., 2013; Reyes et al., 2013; X. Wang & Boudker, 2020). Notably, high, approximately nanomolar apparent binding affinities measured for P-Glt_{Ph} suggest that

substrate dissociation contributes little to the binding process observed in ITC. Thus, the two states may differ primarily in the binding on-rates, with the “high-affinity” state binding substrate faster than the “low-affinity” state. Regardless, these results strongly suggest that there is conformational heterogeneity in the transporter, manifesting in different binding mechanisms.

Different substrate-binding modes have been observed in MD simulations (Alleva et al., 2020; J. Wang, Li, Yu, & Grewer, 2021). However, simulations showed alternate aspartate coordination, which we have not observed in structures. Computational reports also did not document protomer tilts, conformational heterogeneity of the extracellular transport domain regions, and alternate D390 rotamers, which we describe here. Interestingly, a recent saturation transfer difference NMR study examined aspartate binding to liposome-reconstituted Glt_{Ph} and reported an unusually low Hill coefficient of 0.69 (Hall et al., 2020). A Hill coefficient of less than 1 may reflect negative cooperativity between protomers, but it may also result from multiple binding states with distinct affinities.

Recent studies showed that Glt_{Ph}, originating from a hyperthermophilic archaeon, exhibits highly divergent activity modes at ambient temperature, where transporter sub-populations function with rates differing by orders of magnitude (Ciftci et al., 2020). Mutations can produce gain-of-function phenotypes by reducing the population of the “slow” transporters. Switching between the modes is rare, occurring on a time scale of hundreds of seconds and resulting in the so-called static disorder of the transport kinetics. These transport modes were attributed to sub-populations that show different elevator dynamics and intracellular substrate-release rates (Huysmans et al., 2021; Matin et al., 2020). Here, we observed a correlation, where nitrate changes the ratio of different substrate-binding states and increases the fraction of slow WT transporters (**Figure 1f**). Therefore, it is possible that the heterogeneity in the extracellular substrate-binding contributes to the heterogeneous uptake rates or reflects different substrate-binding properties of fast and slow transporter sub-populations. Consistently, R276S/M395R, A345V, and V366A mutations lead to increased elevator dynamics and altered substrate binding (Huysmans et al., 2021), showing that structural perturbations can affect substrate binding and translocation in a concerted fashion.

It is interesting to consider that the substrate-bound transporter prefers the high-affinity OFS state, according to the estimated free energies. In contrast, low- and high-affinity states are similarly populated in the absence of substrate. Thus, the longer the transporter is exposed to the substrate, the more it populates the high-affinity conformation. If so, Glt_{Ph} might undergo ‘hysteresis’ reminiscent of the ABC transporter $BtuC_2D_2$, where prolonged ATP hydrolysis induced a more active transporter state (Livnat-Levanon, A, Ben-Tal, & Lewinson, 2016).

What are the structural differences between the high-affinity S1 and the low-affinity S2? In the P-Glt_{Ph} sample equilibrated in Na^+ and L-Asp (dataset A) and the one equilibrated in Na^+ alone and supplemented with L-Asp seconds before grid freezing (dataset B), we found different global transport domain positions in the OFS, visualized as subtly different rigid-body tilts (**Figure 5**). Earlier double electron-electron resonance (DEER) measurements also suggested that the transport domain is more flexible than appeared from the crystallographic structures (Georgieva et al., 2013; Hanelt, Wunnicke, Bordignon, Steinhoff, & Slotboom, 2013). The mobility of the domain within this state is reminiscent of the large domain movements in the IFS, where the transport domain was observed next to the scaffold or tilting away from it, in the so-called “locked” and “unlocked” states (Akyuz et al., 2015; X. Wang & Boudker, 2020), though movements in the OFS are smaller.

In P-Glt_{Ph} imaged immediately after substrate binding, we observed an overall greater heterogeneity than the pre-equilibrated P-Glt_{Ph} (**Figure 7a-b**). Notably, the transport domains showing different tilts also featured helices in the extracellular half (HP2, TM8a, and TM7b) in a continuum of states. As we did not observe similar helix mobility in the pre-equilibrated structures, we think that the presence of a transient state with more dynamic, less well packed extracellular half of the transport domain is a strong

candidate to explain binding heterogeneity. Consistently, mutations in HP2 that disrupt the hairpin packing with TM8a and TM7b helices and increase local dynamics, V366A and A345V, decrease substrate affinity (Huysmans et al., 2021). In the high-resolution maps of the pre-equilibrated P-Glt_{Ph}, we observed an unusual "up" rotamer of D390, proximal to the substrate-binding site, in a subpopulation of the outward-tilted domains (**Figure 6**). However, the lower resolution of the time-resolved dataset does not allow us to examine whether the correlation between the transport domain tilt and the D390 rotamer holds.

The high-resolution pre-equilibrated structure revealed a network of buried waters, polar residues, and ions in the core of the cytoplasmic half of the transport domain (TM8b, TM7a, HP1) (**Figure 4a**). In contrast, the extracellular half is more hydrophobic and contains no resolved waters. The hydrophobic nature of this protein region may allow for variable helical packing, less constrained by specific polar interactions. Furthermore, S2 corresponding to a less well-packed state of the extracellular transport domain would be consistent with an increased population of the state with temperature and in the presence of the chaotropic salts, conditions favoring greater solvent exposure of the hydrophobic core residues.

Notably, the crystal structures of the substrate-, inhibitor-, and Na^+ only bound OFS (Alleva et al., 2020; Boudker et al., 2007; Yernool, Boudker, Jin, & Gouaux, 2004) picture different conformations of the substrate-binding gate of the transporter, HP2, but also reveal differences in TM8a and TM7b (**Figure 7c**), suggesting that the entire extracellular half of the domain restructures during substrate binding. Consistently, stopped-flow experiments using tryptophan mutants of Glt_{Ph} suggest that simultaneous substrate/Na^+ binding to the transporter involves a kinetically slow step to achieve a tightly bound state, likely after initial binding of sodium (Ewers, Becher, Machtens, Weyand, & Fahlke, 2013; Hanelt et al., 2015). Yet, assays directly following HP2 movements demonstrated that its closure upon substrate binding is rapid (Riederer & Valiyaveetil, 2019). Repacking of the helices could be the kinetically slow step.

Collectively, our data do not allow us to connect low- and high-affinity states to structure unambiguously. Still, there seems sufficient evidence to hypothesize that the packing state of the transport domain determines the slowly exchanging binding states. Regardless, the structural differences are likely small and may require detailed analysis of extremely high-quality cryo-EM datasets to be classified through static structural snapshots. A similar detailed analysis was needed to understand modal gating in KcsA, attributed to subtle sidechain rearrangements and corresponding ion occupancies (Chakrapani et al., 2011). This may apply to other cases of functional heterogeneity in channels, transporters, and enzymes, where proteins sample distinct "modes" with different activities. In particular, single-channel recordings revealed that ligand-gated ion channel nicotinic acetylcholine receptor shows opening bursts interspersed with either short or long closed periods (Colquhoun & Sakmann, 1985), and ionotropic glutamate receptors showed even more complex kinetics with multiple gating modes (Popescu, 2012). P-type ATPase also displayed periods of rapid transport interspersed with prolonged pauses (Veshaguri et al., 2016). As in Glt_{Ph} and KcsA, these distinct modes may be facilitated by subtle structural changes that happen on long timescales.

MATERIALS AND METHODS

DNA manipulations and protein preparation

Mutations were introduced to the previously described Glt_{Ph} CAT7 construct (Yernool et al., 2004) using PfuUltra II, and sequences were verified using Sanger sequencing (Macrogen USA). Proteins were expressed as C-terminal $(His)_8$ fusions, separated by a thrombin cleavage site. Proteins were purified as previously described (Yernool et al., 2004). Briefly, crude membranes of DH10B *E. coli* cells overexpressing Glt_{Ph} were solubilized for 2 hours in 20mM HEPES/NaOH pH 7.4, 200mM NaCl, 5mM

L-Asp, and 40mM n-dodecyl-ß-d-maltopyranoside (DDM, Anatrace). After solubilization, the DDM was diluted to ~8-10 mM, and after a high-speed ultracentrifugation step (40,000 rpm, Ti45 rotor), the supernatant was applied to pre-equilibrated Ni-NTA affinity resin (Qiagen) for 1 hour. The resin was washed with 7 column volumes of 20mM HEPES/NaOH pH 7.4, 200mM NaCl, 5mM L-Asp, and 40mM imidazole. Subsequently, the resin was eluted with the same buffer with increased imidazole (250mM). The $(His)_8$ tag was cleaved by thrombin digestion overnight at 4°C, and the proteins were further purified by size exclusion chromatography (SEC) in the appropriate buffer for subsequent experiments. The concentration of Glt_{Ph} protomers was determined in a UV cuvette with a 10 mm pathlength (Starna Cells, Inc.), using protein diluted 1:40, and an experimentally determined extinction coefficient of 57,400 M^{-1} cm^{-1} (Reyes et al., 2013).

Reconstitution and uptake assays

Liposomes able to maintain proton gradients were prepared using a 3:1 mixture of 1-palmitoyl-2-oleoyl-sn-glycero-3-phosphoethanolamine and 1-palmitoyl-2-oleoyl-sn-glycero-3-phospho-(1'-rac-glycerol) (POPE/POPG). Lipids were dried on the rotary evaporator for 2 hours and under vacuum overnight. The resulting lipid film was hydrated by 10 freeze-thaw cycles at a concentration of 5 mg/mL in a 50 mM potassium phosphate buffer and 100 mM potassium acetate at pH 7. The suspensions were extruded using a Mini-Extruder (Avanti) through 400 nm membranes (Whatman) 10 times to form unilamellar liposomes, then Triton X-100 was added to liposomes at a ratio of 1:2 (w/w).

P-Glt_{Ph} for reconstitution was affinity-purified, thrombin-cleaved, and purified by SEC in 20mM HEPES/Tris pH 7.4, 200mM NaCl, 1mM L-Asp, and 7mM DM. Purified protein was added to destabilized liposomes at a ratio of 1:1000 (w:w) and incubated for 30 min at 23°C. Detergent was removed with four rounds of incubation with SM-2 beads (Bio-Rad) at 80mg beads per 1 mL of liposome suspension (2 hrs at 23°C twice, overnight at 23°C once, and 2 hrs at 23°C once). Prior to use, SM-2 beads were prewashed in methanol, rinsed thoroughly with distilled water, and equilibrated in the liposome internal buffer. After detergent removal, proteoliposomes were concentrated to 50 mg/mL by ultracentrifugation at 86000 x g for 40 min at 4°C, freeze-thawed three times, and extruded through 400 nm membranes 10 times.

Uptakes were initiated by diluting reconstituted proteoliposomes 1:100 in the appropriate reaction buffer pre-incubated at 30°C. At the indicated time points, 200µL reaction aliquots were removed and diluted in 2mL of ice-cold quenching buffer (20mM HEPES/Tris pH 7, 200mM LiCl). The quenched reaction was immediately filtered through a 0.22µm filter membrane (Millipore Sigma) and washed three times with 2mL quenching buffer. Washed membranes were inserted into scintillation vials, and the membranes were soaked overnight in 5 mL Econo-Safe Counting Cocktail. Radioactivity in liposomes was measured using an LS6500 scintillation counter (Beckman Coulter).

Isothermal Titration Calorimetry

Substrate-free P-Glt_{Ph} and Glt_{Ph} proteins were affinity-purified, thrombin-cleaved, and purified by SEC in 20mM HEPES/KOH pH 7.4, 99mM potassium gluconate, 1mM sodium gluconate, and 1mM DDM. Proteins were immediately concentrated to > 5mg/mL and diluted 2.5-fold to a final concentration of 30-50µM. When diluted, the sample was supplemented with a final concentration of 1mM DDM, 58mM HEPES/KOH pH 7.4, and an appropriate amount of sodium salt. 350µL of protein samples were degassed, equilibrated to the temperature of the experiment, and ~300 µL was loaded into the reaction cell of a small volume NanoITC (TA Instruments, Inc.), or in the case of TFB-TBOA experiments, an Affinity Auto ITC (TA Instruments, Inc.). Titrant was prepared in a buffer matching the reaction cell, except that it contained the appropriate amount of monopotassium aspartate (RPI, Inc.) and no protein or DDM. Dilution of DDM in the reaction cell over the course of the experiment had negligible effects on the injection heats, as previously noted (Boudker & Oh, 2015). 2µL of titrant was injected every 5-6

minutes, at a constant temperature, and a stirring rate of 250 rpm (125 rpm for TFB-TBOA experiments). Injection heats measured after protein was saturated with the ligand were used to determine the dilution heats subtracted from the ligand binding heats. Data were analyzed using the NanoAnalyze software (TA Instruments, Inc.) applying either the 'Independent' or 'Multiple Sites' (referred to as 'single-state' and 'two-state' throughout the text) binding models. For the two-state binding, where each state is independent and non-identical, the binding polynomial can be expressed as:

$$\Sigma = 1 + K_1[S] + K_2[S] + K_1K_2[S]^2$$

Where K_i-s are the binding constants, and *[S]* is the concentration of free L-Asp. The fraction of total protein bound is given by the following:

$$\frac{[PS]}{[P]} = \frac{n_1K_1[S]}{1 + K_1[S]} + \frac{n_2K_2[S]}{1 + K_2[S]}$$

where n_i is the apparent number of sites per protein molecule.

For the TFB-TBOA competition experiments, protein was first titrated with TBOA to saturation. Then, the concentration of TFB-TBOA was increased to a final concentration of 150 μM of TFB-TBOA, so that the overflow protein was also saturated. The appropriate amount of aspartate was subsequently titrated into the saturated protein to yield a binding curve.

Cryo-electron microscopy imaging data collection

In both data sets, 3.5 μL of protein at ~4.5 mg/mL was applied to a glow-discharged QuantiFoil R 1.2/1.3, 300 mesh, gold grid (Electron Microscopy Sciences). Grids were blotted at room temperature and 100% humidity for 3 s at 0 blot force, and plunge frozen in liquid ethane using a VitroBot Mark VI (FEI). Dataset A was collected on P-Glt_{Ph} SEC purified in 20mM HEPES/Tris pH 7.4, 250 mM $NaNO_3$, 1mM L-Asp, and 0.8mM DDM. Dataset B was collected on P-Glt_{Ph}, which was affinity-purified, concentrated, and buffer-exchanged into 20mM HEPES/Tris pH 7.4, 99mM K-gluconate, 1mM Na-gluconate, and 0.8mM DDM to remove the substrate. The protein was then SEC purified in 20mM HEPES/Tris pH 7.4, 250mM $NaNO_3$, and 0.8mM DDM. 2.5 μL of substrate-free protein was applied to the grid, then 1μL of L-aspartate was added and mixed just prior to freezing so that the final substrate concentration was 1mM, the final protein concentration was ~4.5mg/mL, and protein was exposed to the substrate for ~5s prior to freezing (including blot time). The final buffer conditions of Dataset B were identical to Dataset A.

All imaging data were collected on Titan Krios microscopes (FEI) operated at 300 kV. Dataset A was collected with a K3 Summit direct electron detector (Gatan). Automated data collection was performed in super-resolution counting mode using SerialEM software (Mastronarde, 2005) with a magnification of 81000x, electron exposure of 47.91 $e^-/Å^2$, 30 frames per second, a defocus range of -0.5 to -2.5 μm, and pixel size of 0.53 Å/pix. Dataset B was collected on a K2 Summit direct electron detector (Gatan). Automated data collection was performed in counting mode using Leginon software (Suloway et al., 2005), with a magnification of 22500x, electron exposure of 70.23 $e^-/Å^2$, 50 frames per second, a defocus range of -1.0 to -2.0 μm, and pixel size of 1.073 Å/pix.

Image processing

The frame stacks were motion-corrected using MotionCor2 (Zheng et al., 2017), with 2x binning in the case of Dataset A, and contrast transfer function (CTF) estimation was performed using CTFFIND 4.1 (Rohou & Grigorieff, 2015). All datasets were processed using cryoSPARC 3.0 and Relion 3.0.8 simultaneously with default parameters unless otherwise stated (Punjani, Rubinstein, Fleet, &

Brubaker, 2017; Su et al., 2020; Zivanov et al., 2018). Specific information on the processing of each dataset is in **Figure 2 – Supplementary Figures 2-4**. In brief, particles were non-specifically picked from micrographs using the Laplacian-of-Gaussian (LoG) picker, aiming for ~2000 picks per micrograph. These particles were extracted at a box size of 240 pixels with 4x binning. These particles were then imported to cryoSPARC, underwent one round of 2D classification to remove artifacts, and then multiple rounds of heterogeneous refinement (C1) using eight total classes, seven of which were noisy volumes (created by one iteration of *ab initio*) and one of which were an unmasked 3D model obtained from a previous processing pipeline. Once > 95% of particles converged on a single class, the particles were converted back to Relion format via PyEM (Asarnow, Palovcak, & Cheng, 2019), and re-extracted at full box size. These particles were reimported to cryoSPARC, underwent three more rounds of heterogeneous refinement, then non-uniform (NU) refinement using C3 symmetry (dynamic mask threshold, dynamic mask near, and dynamic mask far were always set to 0.8, 12, and 28, respectively) (Punjani, Zhang, & Fleet, 2020). These particles were converted back to Relion format and underwent Bayesian polishing, using parameters obtained using 5,000 random particles within the set. After three more rounds of heterogeneous refinement in cryoSPARC and one round of NU-refinement, we performed local CTF refinement (minimum fit res 7 Å). After three more rounds of heterogeneous refinement and one round of NU-refinement, we performed global CTF refinement (3 iterations, minimum fit res 7 Å; fitting trefoil, spherical aberration, and tetrafoil), three more rounds of heterogeneous refinement, and one round of NU-refinement.

Dataset A was also further processed to obtain the high-resolution structure by three additional rounds of polishing, local CTF refinement, and global CTF refinement as described above. During the polishing rounds, the box size and pixel size was rescaled as indicated in the supplement. After the second round of polishing, we classified single protomers by employing the 'relion_particle_symmetry_expand' function in Relion to artificially expand the particle set three times (C3) so that each protomer rotated to the same position (Scheres, 2016). The expanded particle set was subjected to 3D classification without alignment with T=400 and 10 classes, using the refined C3 structure as a reference map. The exceptionally high T value was chosen to separate out subtle structural changes, and lower T values were also tested during processing. The local mask was created using a 20 Å map of the transport domain of Chain A of PDB model 2NWX, with an initial binarization threshold of 0.01, extended by 3 pixels, and a soft-edge of 10 pixels. Of these, particle stacks from subsets of interest were separately used in cryoSPARC's local refinement (C1), using the mask and map obtained from the most recent NU-refinement. Single protomers in Dataset B were classified similarly, except we performed symmetry expansion after the first round of polishing due to the limited resolution of the dataset. After processing, the resulting half-maps were used as inputs for density modification implemented in PHENIX 1.19.1-4122 (Adams et al., 2010; Terwilliger, Ludtke, Read, Adams, & Afonine, 2020), using a mask created from the NU-refinement job (threshold 0.1, dilation radius 15, soft padding width 5). All density maps were displayed using ChimeraX (Pettersen et al., 2021).

Model building and refinement

For atomic model building, the crystal structure of WT Glt_{Ph} in the OFS (2NWX) was docked into the densities using UCSF Chimera (Pettersen et al., 2004). The model was first real-space refined in PHENIX (Adams et al., 2010). Then, chain A was adjusted manually, and ions were added in COOT (Emsley & Cowtan, 2004). Waters were initially added using phenix.douse, and subsequently manually inspected and adjusted. The resulting model underwent additional rounds of real-space refinement and validated using MolProbity (Chen et al., 2010). All structural models were displayed using ChimeraX (Pettersen et al., 2021). Per-residue Cα RMSDs were generated with Chimera (Meng, Pettersen, Couch, Huang, & Ferrin, 2006). To cross-validate models, refined models (FSC_{sum}) were randomly displaced an average of 0.3 Å using phenix.pdbtools. The displaced model was real-space refined against half-map 1 obtained through density modification to obtain FSC_{work}. The resulting model was validated against half-map 2 to obtain FSC_{free}.

Single-molecule dynamics assay

Thrombin-cleaved P-Glt_{Ph}, containing C321A and N378C mutations, was labeled and reconstituted as described previously (Akyuz et al., 2013). Protein was SEC purified in 20 mM HEPES/Tris, 200 mM NaCl, 1 mM L-Asp, and 1 mM DDM. Purified protein was labeled using maleimide-activated LD555P-MAL and LD655-MAL dyes and biotin-PEG_{11} at a molar ratio of 4:5:10:2.5. Excess dyes were removed on a PDMiniTrap Sephadex G-25 desalting column (GE Healthcare).

All experiments were performed on a previously described home-built prism-based TIRF microscope constructed around a Nikon Eclipse Ti inverted microscope body (Juette et al., 2016). Microfluidic imaging chambers were passivated with biotin-PEG, as previously described (Akyuz et al., 2015). After passivation, the microfluidic channel was incubated with 0.8 μM streptavidin (Invitrogen) in T50 buffer (50 mM NaCl, 10 mM Tris, pH 7.5) for 7 min, then thoroughly rinsed with T50 buffer. Detergent-solubilized protein was immobilized by slowly flowing over the channel, and excess protein was removed by washing with 1 mL 25 mM HEPES/Tris pH 7.4, 200 mM KCl, 1 mM DDM.

Buffers were supplemented with an oxygen-scavenging system composed of 2 mM protocatechuic acid (PCA) and 50 nM protocatechuate-3,4-dioxygenase (PCD), as described previously (Aitken, Marshall, & Puglisi, 2008). The smFRET movies were recorded with 100 ms integration time using 80-100 mW laser power. All conditions tested were in the presence of 25 mM HEPES/Tris, 500 mM sodium salt, and 1 mM DDM, either in the presence or absence of 1 mM L-Asp. Slides were washed with 25 mM HEPES/Tris, 200 mM KCl, 1 mM DDM between experiments. Traces were analyzed using the Spartan software (Juette et al., 2016). Trajectories were corrected for spectral crosstalk and preprocessed automatically to exclude trajectories that lasted 15 or fewer frames and had a signal-to-noise ratio of 8 or lower. Traces with multiple photobleaching events (indicative of multiple sensors in a protein) or inconsistent total fluorescence intensity were also discarded.

Single-molecule transport assay and analysis

Thrombin-cleaved Glt_{Ph} (C321A/N378C) was SEC purified in 20 mM HEPES/Tris pH 7.4, 200 mM NaCl, and 0.1 mM L-Asp. Protein was labeled with maleimide-activated biotin-PEG_{11} (EZ-Link, ThermoFisher Scientific) in the presence of *N*-ethylmaleimide (NEM) at a molar ratio of 1:2:4 as previously described (Ciftci et al., 2020). Liposomes were prepared from a 3:1 (w:w) mixture of *E. coli* polar lipid extract (Avanti Polar Lipids, Inc.) and egg phosphatidylcholine in SM-KCl buffer (50 mM HEPES/Tris pH 7.4, 200 mM KCl). Liposomes were extruded through 400-nm filters (Whatman Nucleopore) using a syringe extruder (Avanti), and destabilized by the addition of Triton X-100 at 1:2 (w:w) detergent-to-lipid ratio. Labeled Glt_{Ph} was added to the liposome suspension at 1:1000 (w:w) protein-to-lipid ratio at room temperature for 30 min. Detergent was removed by six rounds incubation of Bio-Beads (two rounds at 23°C for 2 hours each, one round at 4°C overnight, three rounds at 4°C for 2 hours each). The excess substrate was removed by three rounds of: centrifugation for 1 hour at 49,192 x g at 4°C, removal of the supernatant, the addition of 1mL fresh SM buffer, and three freeze/thaw cycles. Liposomes were concentrated to 50 mg/mL, and ccPEB1a-Y198F labeled with activated LD555P-MAL and LD655-MAL dyes as described (Ciftci et al., 2020) was added at a final concentration of 0.6 μM and encapsulated by two freeze-thaw cycles. To remove unencapsulated ccPEB1a-Y198F, 1 mL of SM-KCl buffer was added, and liposomes were centrifuged for 1 hour at 49.192 x g at 4°C. Supernatants were discarded, liposomes were suspended at 50 mg/mL, and extruded 12 times through 100-nm filters.

Single-transporter smFRET assays were performed on the same microscope described above, and the microfluidic imaging chambers were prepared in the same way. After coating with streptavidin, the channel was rinsed thoroughly with SM-K(X) buffer (50 mM HEPES/Tris pH 7.4 containing 200 mM potassium salt buffer, where the anion (X) was changed based on the condition tested). Extruded liposomes were immobilized by slowly flowing over the channel, and excess liposomes were removed

by washing with 1 mL SM-K(X) buffer.

Buffers were supplemented with an oxygen-scavenging system as above, and the smFRET movies were recorded with 400 ms integration time using 20-40 mW laser power. To confirm liposomes were not leaky, a movie was taken in SM-K(X) buffer containing 1 μM L-Asp and 1 μM valinomycin. No L-Asp uptake was observed under these conditions lacking Na^+ gradient. After completion of this movie, another movie was initiated to record transport events. At approximately 3 seconds into this movie, SM-Na(X) buffer containing 1 μM L-Asp and 1 μM valinomycin was perfused into the channel.

Traces were analyzed using the Spartan software (Juette et al., 2016). Trajectories were corrected for spectral crosstalk and preprocessed automatically to exclude trajectories that lasted 15 or fewer frames, had a signal-to-noise ratio of 8 or lower, and had an initial FRET efficiency less than 0.4 or greater than 0.7. Traces with multiple photobleaching events (indicative of multiple sensors in a liposome) or inconsistent total fluorescence intensity were also discarded. Remaining traces were sorted by either the presence or absence of observable transport events (responding and non-responding traces, respectively), determined by an increase in FRET efficiency from ~0.55-0.6 to ~0.75-0.8.

Responding traces from each movie were plotted as time-dependent mean FRET efficiency. Buffer replacement time was determined as described (Ciftci et al., 2020). Within each dataset, the data was normalized so that 0% is the first time point, and 100% is the first time point + 0.2 (the change in FRET efficiency upon saturation of ccPEB1a-Y198F). The resulting normalized data were multiplied by the fraction of the responding traces relative to the total traces. Data from three independent reconstitutions were merged and fitted to a tri-exponential function in GraphPad Prism 8.4.2, where Y0 = 0, Plateau = 1, percentages were set between 0 and 100, and all rate constants were set to be shared between all data sets and greater than zero.

ACKNOWLEDGEMENTS

We thank Eva Fortea, Navid Paknejad, and Drs. Maria Falzone, Philipp Schmidpeter, Biao Qiu, and Xiaoyu Wang for helpful discussions on cryo-EM data processing. Also, we thank Bryce Delgado for preliminary ITC experiments, Will Eng for protein expression, and Vishnu Ghani for preparation of the PEB1a protein. We thank Dr. Scott Blanchard and members of the Blanchard lab for support and resources for smFRET experiments. Finally, we thank Erika Riederer and Dr. Francis Valiyaveetil for helpful discussions and exploratory experiments. The work was supported by NIH F32 NS102325 (to KDR), AHA 19PRE34380215 (to DC), and NIH R01NS064357 and R37NS085318 (to OB). Dataset A was collected at the UMass cryo-EM facility with help from Dr. Kangkang Song and Dr. Chen Xu. Dataset B was collected with assistance from Carolina Hernandez at the Simons Electron Microscopy Center and National Resource for Automated Molecular Microscopy located at the New York Structural Biology Center, supported by grants from the Simons Foundation (349247), NYSTAR, and the NIH National Institute of General Medical Sciences (GM103310) with additional support from Agouron Institute (F00316) and NIH S10 OD019994-01.

COMPETING INTERESTS

None.

AUTHOR CONTRIBUTIONS

K.D.R. and O.B. designed the experiments, analyzed the data, refined the molecular models, and wrote the manuscript with input from all authors. K.D.R. and A.S. performed the cloning and radioactive transport assays. K.D.R. and D.C. performed the smFRET dynamics and transport assays. K.D.R. performed the ITC and cryo-EM sample preparation and processing.

SUPPLEMENTARY INFORMATION

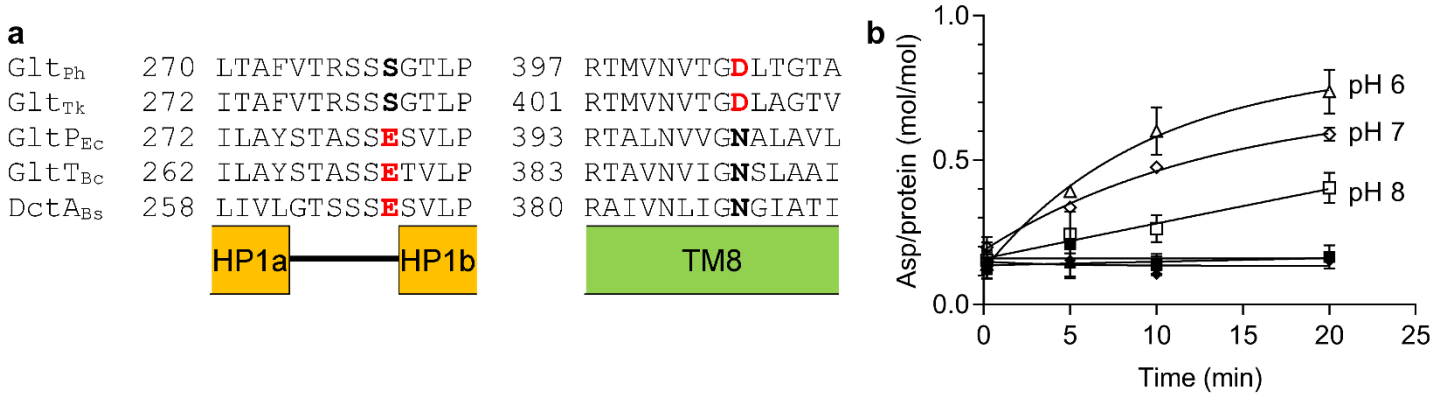

Figure 1 - Supplementary Figure 1. P-Glt$_{Ph}$ (S279E/D405N) has partial proton dependence. (a) Sequence alignment of Na^+-coupled (Glt$_{Ph}$, Glt$_{Tk}$) and H^+-coupled (GltP$_{Ec}$, GltT$_{Bc}$, DctA$_{Bs}$) transporters; structural elements are indicated below the alignment. Residues mutated in P-Glt$_{Ph}$ are in bold. (b) pH-dependent aspartate uptake of P-Glt$_{Ph}$. Proteoliposomes were loaded with 50 mM potassium phosphate buffer, pH 7, and 100 mM potassium acetate and diluted into the following 50 mM buffers containing 1 µM ^{3}H-L-Asp: MES/NMDG pH 6 (triangles), HEPES/Tris pH 7 (diamonds), or HEPES/Tris pH 8 (squares). Buffers contained either 100 mM KCl (filled symbols) or 100 mM NaCl (empty symbols). Solid lines are shown to guide the eye, and error bars (SD) not displayed represent errors smaller than the size of the symbol.

Trial	n_1	$K_{D,1}$ (M)	ΔG_1 (kcal mol^{-1})	ΔH_1 (kcal mol^{-1})	ΔS_1 (cal mol^{-1} K^{-1})	n_2	$K_{D,2}$ (M)	ΔG_2 (kcal mol^{-1})	ΔH_2 (kcal mol^{-1})	ΔS_2 (cal mol^{-1} K^{-1})	% n_2
1	0.61	2.3e-9	-11.35	-2.06	32.2	0.13	1.3e-7	-8.98	-6.00	10.3	18
2	0.64	1.0e-10	-13.15	-1.64	40.0	0.20	5.5e-9	-10.81	-4.73	21.1	24
3	0.78	3.6e-9	-11.10	-2.13	31.1	0.18	1.1e-7	-9.07	-6.35	9.4	19
avg			**-11.86 ± 0.91**	**-1.94 ± 0.22**	**34.4 ± 3.9**			**-9.62 ± 0.84**	**-5.70 ± 0.69**	**13.6 ± 5.3**	**20 ± 3**

Figure 2 – Supplementary Table 1. L-Asp binding to P-Glt$_{Ph}$ (S279E/D405N) at 10°C in 500 mM NaCl. Binding parameters are from fits to the two-state model. Averaged values are means and standard deviations from three independent experiments.

Trial	n_1	$K_{D,1}$ (M)	ΔG_1 (kcal mol^{-1})	ΔH_1 (kcal mol^{-1})	ΔS_1 (cal mol^{-1} K^{-1})	n_2	$K_{D,2}$ (M)	ΔG_2 (kcal mol^{-1})	ΔH_2 (kcal mol^{-1})	ΔS_2 (cal mol^{-1} K^{-1})	% n_2
1	1.13	1.9e-9	-11.51	-3.05	29.4	0.39	3.9e-8	-9.77	-6.63	10.9	26
2	0.64	1.3e-9	-11.73	-3.31	29.2	0.22	6.1e-8	-9.51	-7.13	8.3	26
3	0.63	3.4e-9	-11.17	-2.11	31.4	0.29	1.7e-8	-10.23	-9.04	4.2	31
avg			**-11.47 ± 0.23**	**-2.82 ± 0.52**	**30.0 ± 1.0**			**-9.84 ± 0.30**	**-7.60 ± 1.04**	**7.8 ± 2.8**	**28 ± 3**

Figure 2 – Supplementary Table 2. L-Asp binding to P-Glt$_{Ph}$ (S279E/D405N) at 15°C in 500 mM NaCl. Binding parameters were fitted to the two-state model. Averaged values are means and standard deviations from three independent experiments.

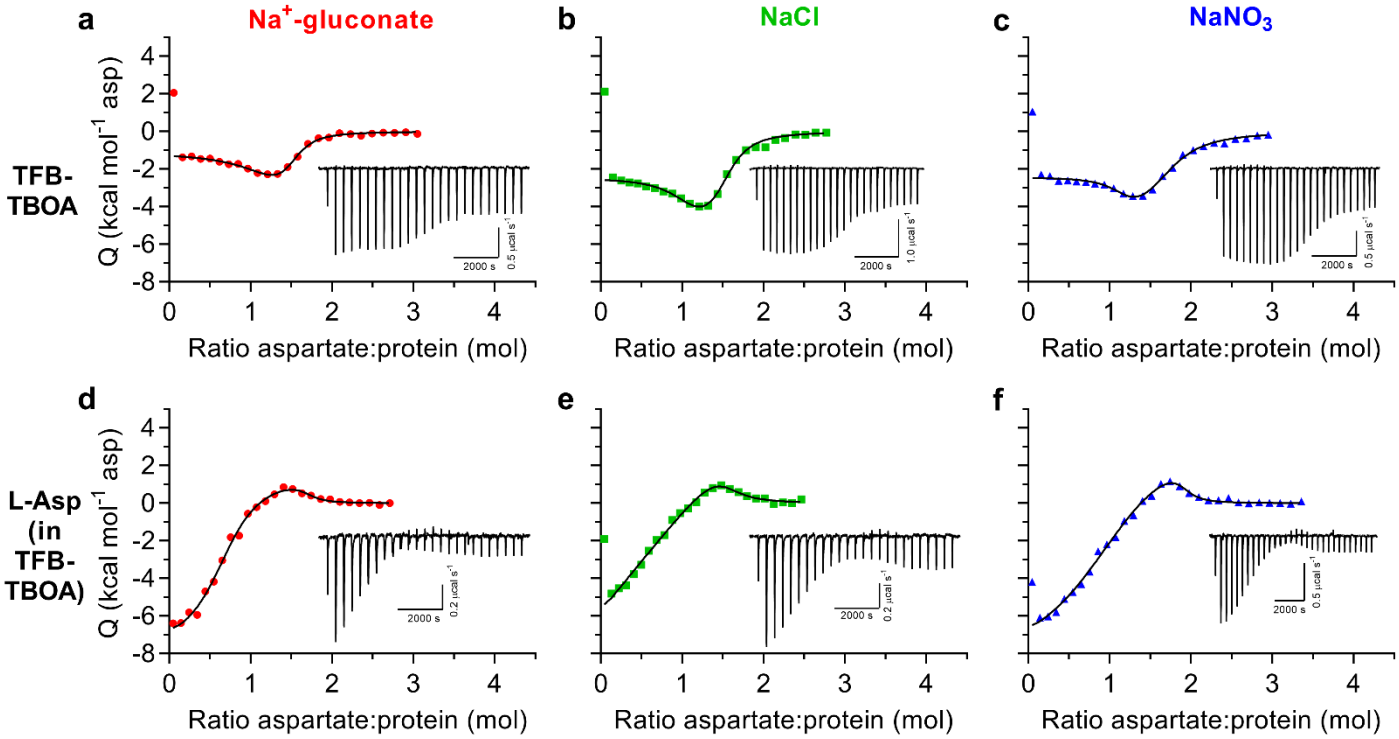

Figure 3 - Supplementary Figure 1. TFB-TBOA binds to two states in WT Glt_{Ph}. All ITC experiments were performed at 15°C in buffers containing 500 mM Na-gluconate (red circles), NaCl (green squares), or $NaNO_3$ (blue triangles). Insets show the thermal power with the corresponding scales. All data were fitted to the two-state model; however, exact binding parameters cannot be reliably determined. (a-c) TFB-TBOA binding isotherms. (d-f) Aspartate competition isotherms in the presence of saturating TFB-TBOA concentrations (Methods).

	Turnover (s^{-1})	Na-gluconate (%)	NaCl (%)	$NaNO_3$ (%)
Fast	2.0 ± 0.5	12.5 ± 1.7	13.1 ± 1.9	9.1 ± 1.1
Intermediate	14.7 ± 7.4	6.4 ± 1.4	7.5 ± 1.6	3.6 ± 1.1
Slow	5227 ± 3612	81.1 ± 3.1	79.5 ± 3.4	87.3 ± 2.2

Figure 3 - Supplementary Table 1. Fitted parameters of L-Asp uptake by WT Glt_{Ph} in the presence of various anions. Data in Figure 3e-f were fitted to a tri-exponential function (a three-phase association model, GraphPad Prism). Initial and final fractions of total possible uptake were set to 0 and 1, respectively. The three turnover rates (fast, intermediate, and slow), corresponding to the heterogeneous transporter populations, were constrained to be the same for all datasets (see *Methods* for a detailed description of data processing). Three independent experiments per condition were analyzed, and shown values are means and SE of the fitted parameters.

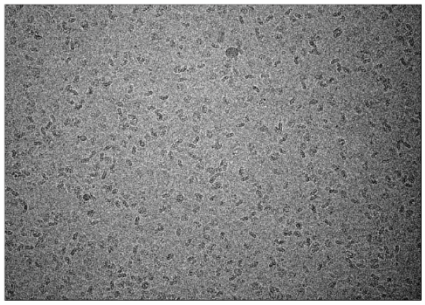

2,904 micrographs, 0.53 Å/pixel
MotionCor2, 2x binning
CTFFIND 4.1
LoG picking
9,234,348 particles

Extract with 4x binning

Heterogeneous refinement (3x)
1,118,273 particles

Unbin to 1.06 Å/pixel

Heterogeneous refinement (3x)
NU-refinement
Remove duplicates, re-center
686,169 particles
NU-refinement (C3)

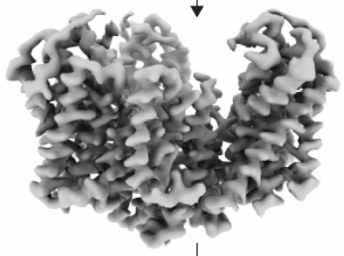

2.78 Å

Bayesian polishing
Heterogeneous refinement (3x)
NU-refinement (C3)
Local CTF Refine
Heterogeneous refinement (3x)
NU-refinement (C3)
Global CTF Refine
Heterogeneous refinement (3x)
621,808 particles
NU-refinement (C3)

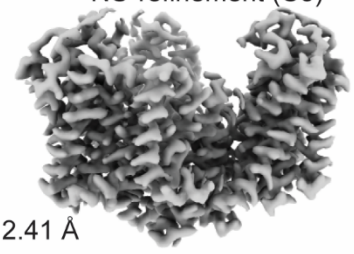

2.41 Å

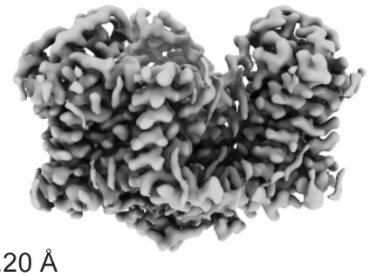

2.20 Å

Bayesian polishing
(448 pix box size, 0.81 Å/pix)
Heterogeneous refinement (3x)
503,427 particles
NU-refinement (C3) w/
local and global CTF refinement

Symmetry expansion and focused classification continued on Fig. 5, Supp. 1

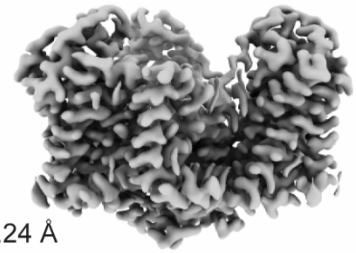

2.24 Å

Bayesian polishing
(384 pix box size, 0.83 Å/pix)
Heterogeneous refinement (3x)
541,152 particles
NU-refinement (C3) w/
local and global CTF refinement

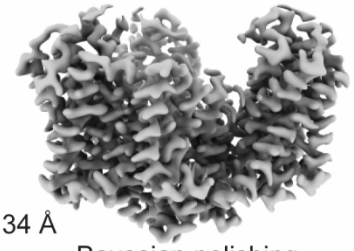

2.34 Å

Bayesian polishing
(360 pix box size, 0.67 Å/pix)
Heterogeneous refinement (3x)
NU-refinement (C3)
Local CTF Refine
Heterogeneous refinement (3x)
NU-refinement (C3)
Global CTF Refine
Heterogeneous refinement (3x)
609,474 particles
NU-refinement (C3)

Figure 4 - Supplementary Figure 1. Processing flowchart for Dataset A. Unsharpened maps are contoured at σ of 8.

	$P\text{-}Glt_{Ph}$ OFS	$P\text{-}Glt_{Ph}$ OFS_{out}	$P\text{-}Glt_{Ph}$ OFS_{out}	$P\text{-}Glt_{Ph}$ OFS_{mid}	$P\text{-}Glt_{Ph}$ OFS_{in}
D390 state		down	up	down	down
Cryo-EM acquisition and processing					
EMDataBank ID	EMD-24405	EMD-24405	EMD-24405	EMD-24405	EMD-24405
Symmetry imposed	C3	C1	C1	C1	C1
Initial particles	9,234,148	1,620,456	1,620,456	1,620,456	1,620,456
Final particles	503,427	78,248	80,207	243,208	142,738
Resolution (masked FSC = 0.143, Å)	2.20	2.56	2.61	2.37	2.40
Density modified CC (0.5, Å)	2.20	2.56	2.59	2.33	2.39
Model Refinement					
PDB ID	7RCP				
Model resolution (FSC = 0.50/0.143 Å)	2.23 / 2.01	2.60 / 2.08	2.66 / 2.04	2.36 / 1.92	2.42 / 2.00
Model composition					
Non-hydrogen atoms	9339	9294	9294	9306	9307
Protein residues	1248	1246	1246	1246	1245
Ligands	6	6	6	6	6
Waters	57	29	31	41	49
R.m.s. deviations					
Bond lengths (Å)	0.005	0.003	0.003	0.004	0.003
Bond angles (°)	0.620	0.494	0.488	0.618	0.550
Validation					
MolProbity score	1.18	1.26	1.38	1.07	1.15
Clash score	3.88	5.00	5.52	2.79	3.58
Poor rotamers (%)	0	0	0	0	0
Ramachandran plot					
Favored (%)	98.79	98.54	98.62	98.62	98.78
Allowed (%)	1.21	1.26	1.38	1.38	1.22
Disallowed (%)	0	0	0	0	0

Figure 4 – Supplementary Table 1. Model refinement and validation statistics for Dataset A.

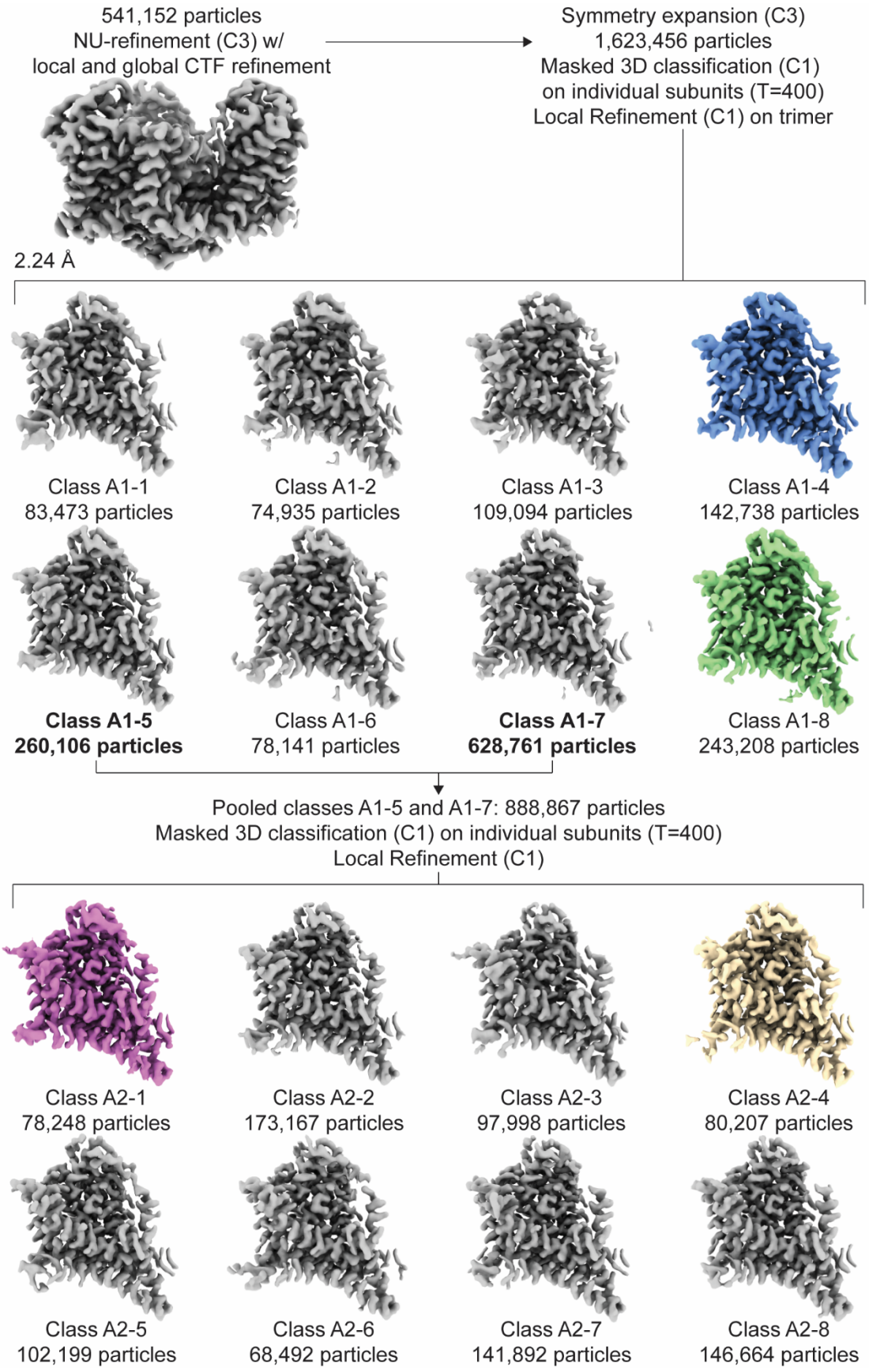

Figure 5 - Supplementary Figure 1. Focused classification of dataset A. Protomers from masked classification are unsharpened, with the two other protomers removed for clarity. Colored structures were used for further model refinement (blue: OFS_{in}; green: OFS_{mid}; purple: OFS_{out}, D390 down; wheat: OFS_{out}, D390 up). All structures have a σ of 8.

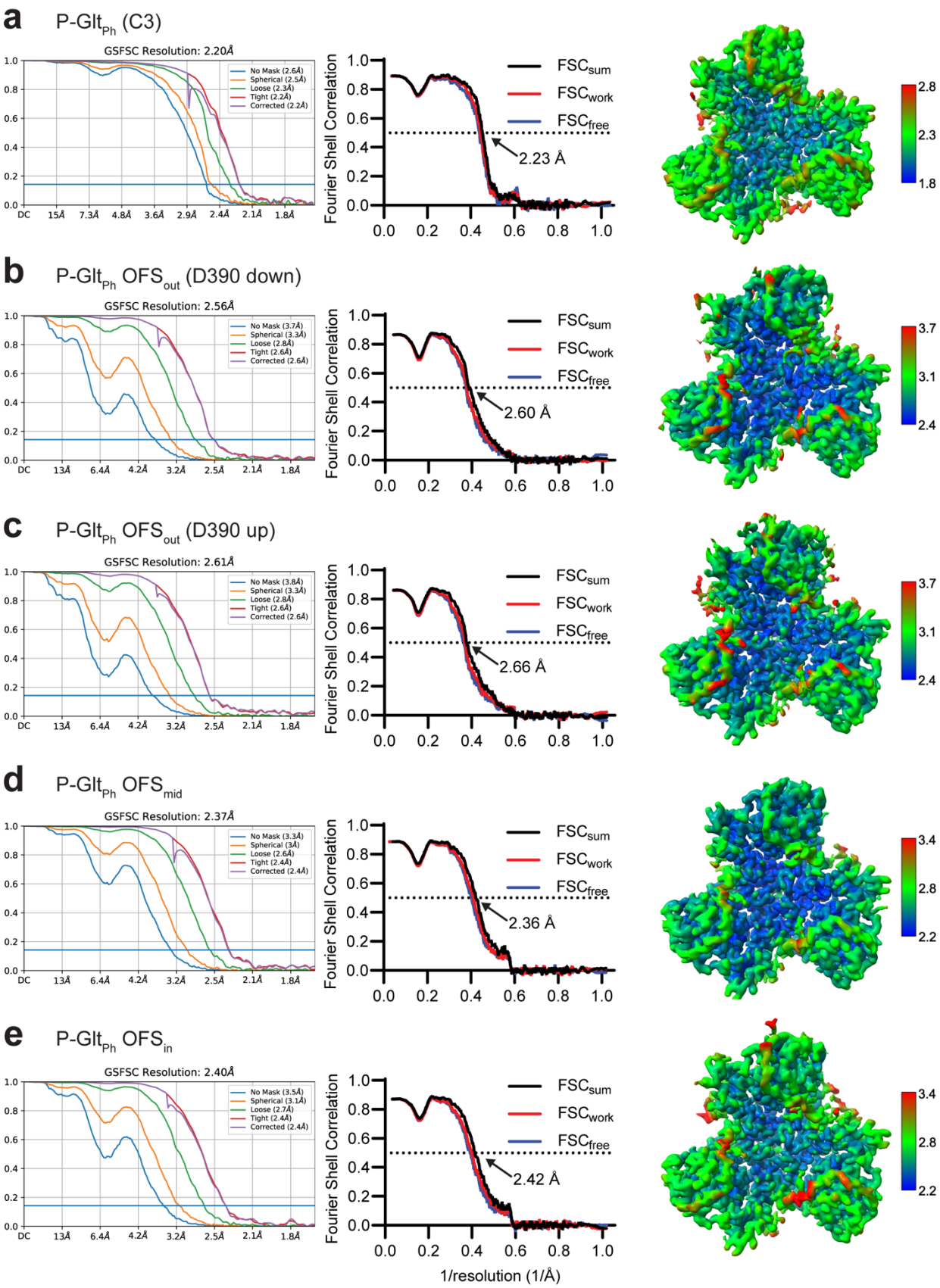

Figure 4 - Supplementary Figure 2. Validation statistics for models from Dataset A. (a) OFS-C3; (b) OFS$_{out}$, D390 down; (c) OFS$_{out}$, D390 up; (d) OFS$_{mid}$; (e) OFS$_{in}$. From left to right, map FSC from NU-refinement in cryoSPARC, model-to-data validation in Phenix of the trimer, and local resolution estimation. All structures have a σ of 8 except (A), which has a σ of 10. The top protomer in (B-E) is the subject of focused classification and model refinement.

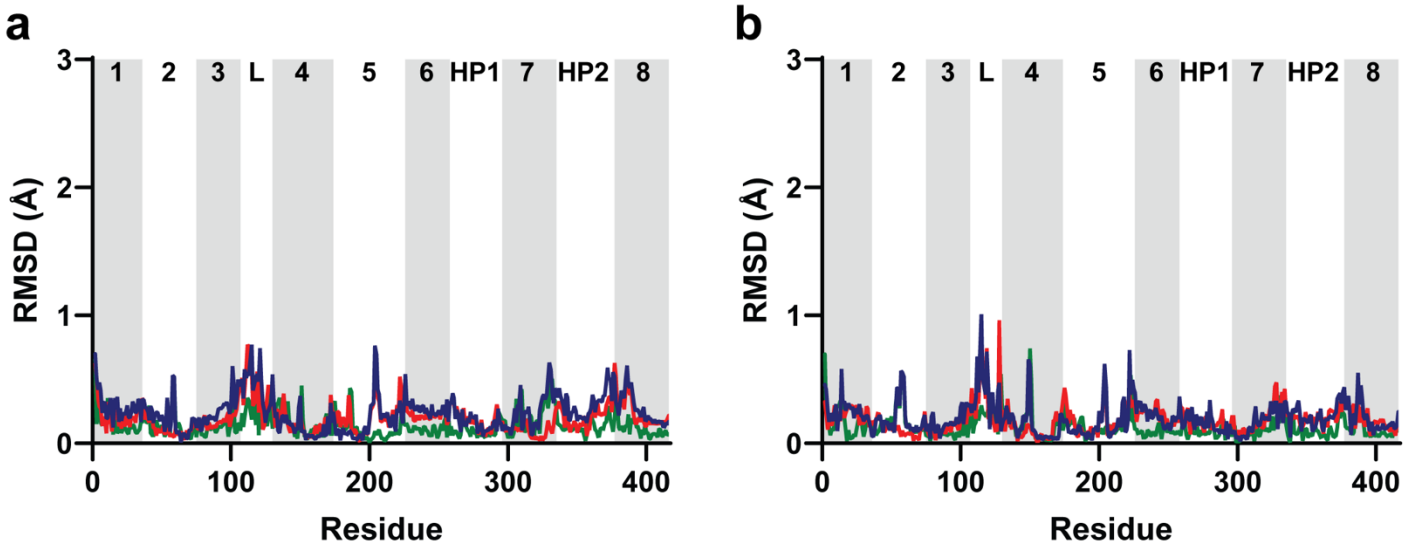

Figure 5 – Supplementary Figure 2. Protomers adjacent to chain A do not display concerted movements. Trimers were aligned along the trimerization regions of all three protomers (residues 150-195). Per-residue Cα RMSDs of (a) chain B, and (b) chain C. Lines are (green) OFS_{out}/OFS_{mid}; (red) OFS_{mid}/OFS_{in}; and (blue) OFS_{out}/OFS_{in}. Transmembrane domains are labeled and alternatively shaded. 'L' indicates the disordered loop between domains 3 and 4.

Structure	RMSD (Å) compared to 2NWX
OFS_{out}	0.475
OFS_{mid}	0.446
OFS_{in}	0.449

Figure 5 – Supplementary Table 1. Comparison between tilt states and a previous crystal structure of substrate-bound, outward-facing state. RMSD was determined using 'matchmaker' implemented in ChimeraX using default parameters. Residues 12-106, 130-416 were used for alignment to include only well-structured, well-resolved regions.

Class (Round 1)	Tilt state	D390 rotamer	Class (Round 2)	Tilt state	D390 rotamer
A1-1	OFS_{out}	intermediate	A2-1	OFS_{out}	down
A1-2	OFS_{mid}	unresolved	A2-2	OFS_{mid}	unresolved
A1-3	OFS_{mid}	down	A2-3	OFS_{mid}	down
A1-4	OFS_{in}	down	A2-4	OFS_{out}	up
A1-5	**OFS_{out}**	**ambiguous**	A2-5	OFS_{mid}	unresolved
A1-6	OFS_{mid}	down	A2-6	OFS_{mid}	down
A1-7	**OFS_{mid}**	**ambiguous**	A2-7	OFS_{in}	down
A1-8	OFS_{mid}	down	A2-8	OFS_{mid}	down

Figure 6 – Supplementary Table 1. Correlation of tilt states and D390 rotamers from Dataset A processing.

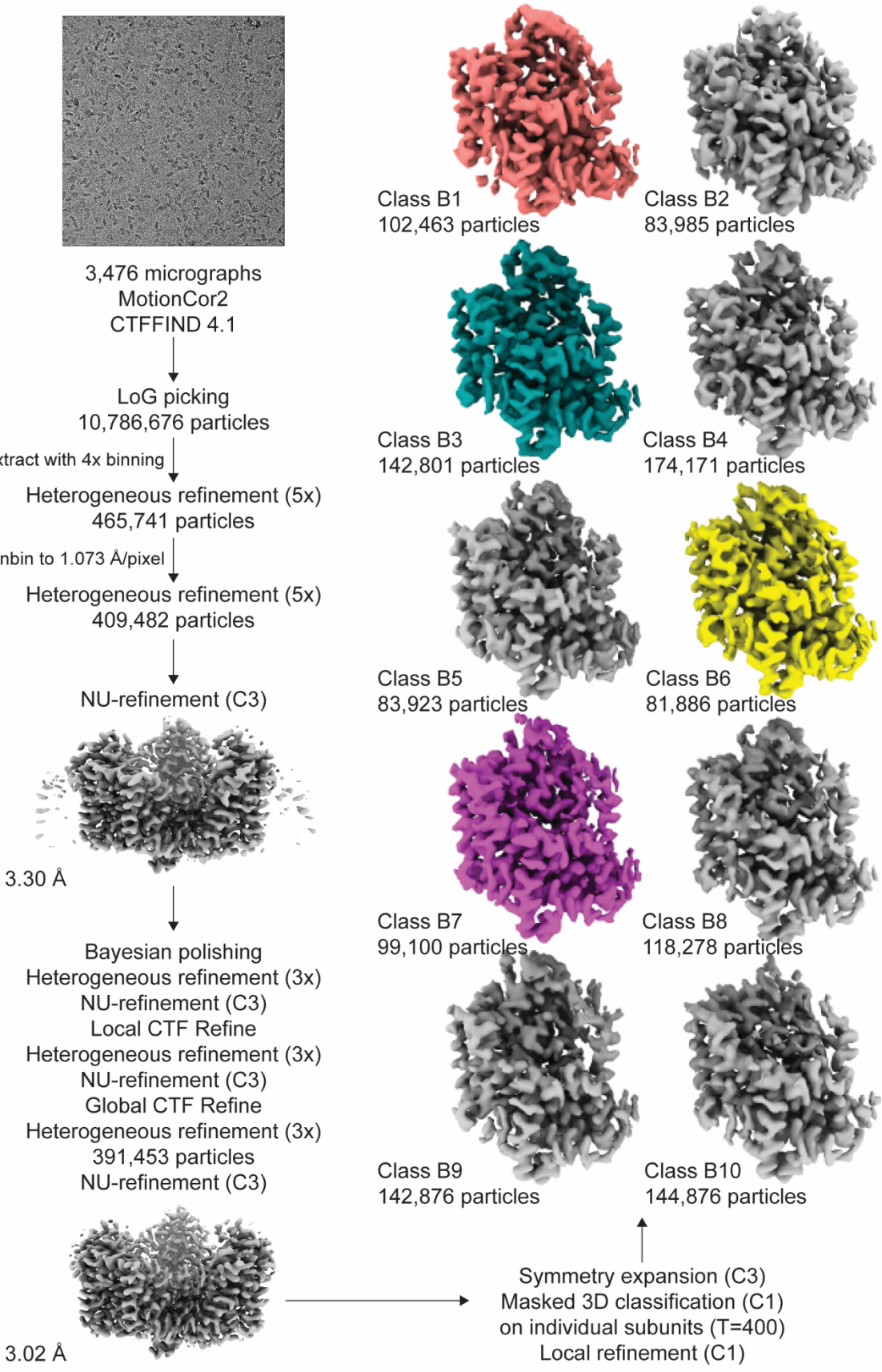

Figure 7 - Supplementary Figure 1. Processing flowchart for Dataset B. Protomers from masked classification are unsharpened, with the two other protomers removed for clarity. All structures have a σ of 8.

	$P\text{-}Glt_{Ph}$ B1	$P\text{-}Glt_{Ph}$ B3	$P\text{-}Glt_{Ph}$ B6	$P\text{-}Glt_{Ph}$ B7
Cryo-EM acquisition and processing				
EMDataBank ID	EMD-24406	EMD-24406	EMD-24406	EMD-24406
Symmetry imposed	C1	C1	C1	C1
Initial particles	1,174,359	1,174,359	1,174,359	1,174,359
Class number	B1	B3	B6	B7
Final particles	102,463	142,081	81,886	99,100
Resolution (masked FSC = 0.143, Å)	3.42	3.06	3.65	3.53
Density modified CC (0.5, Å)	3.45	3.09	3.64	3.57
Model Refinement				
Model resolution (FSC = 0.50/0.143 Å)	3.55 / 3.08	3.15 / 2.63	3.85 / 3.35	3.76 / 3.32
Model composition				
Non-hydrogen atoms	3097	3094	3094	3094
Protein residues	416	416	416	416
Ligands	2	2	2	2
R.m.s. deviations				
Bond lengths (Å)	0.003	0.002	0.003	0.003
Bond angles (°)	0.486	0.462	0.578	0.523
Validation				
MolProbity score	1.42	1.21	1.58	1.78
Clash score	6.93	4.41	10.55	10.55
Poor rotamers (%)	0	0	0	0
Ramachandran plot				
Favored (%)	97.82	98.79	97.82	96.37
Allowed (%)	2.18	1.21	2.18	3.63
Disallowed (%)	0	0	0	0

Figure 7 – Supplementary Table 1. Model refinement and validation statistics for Dataset B.

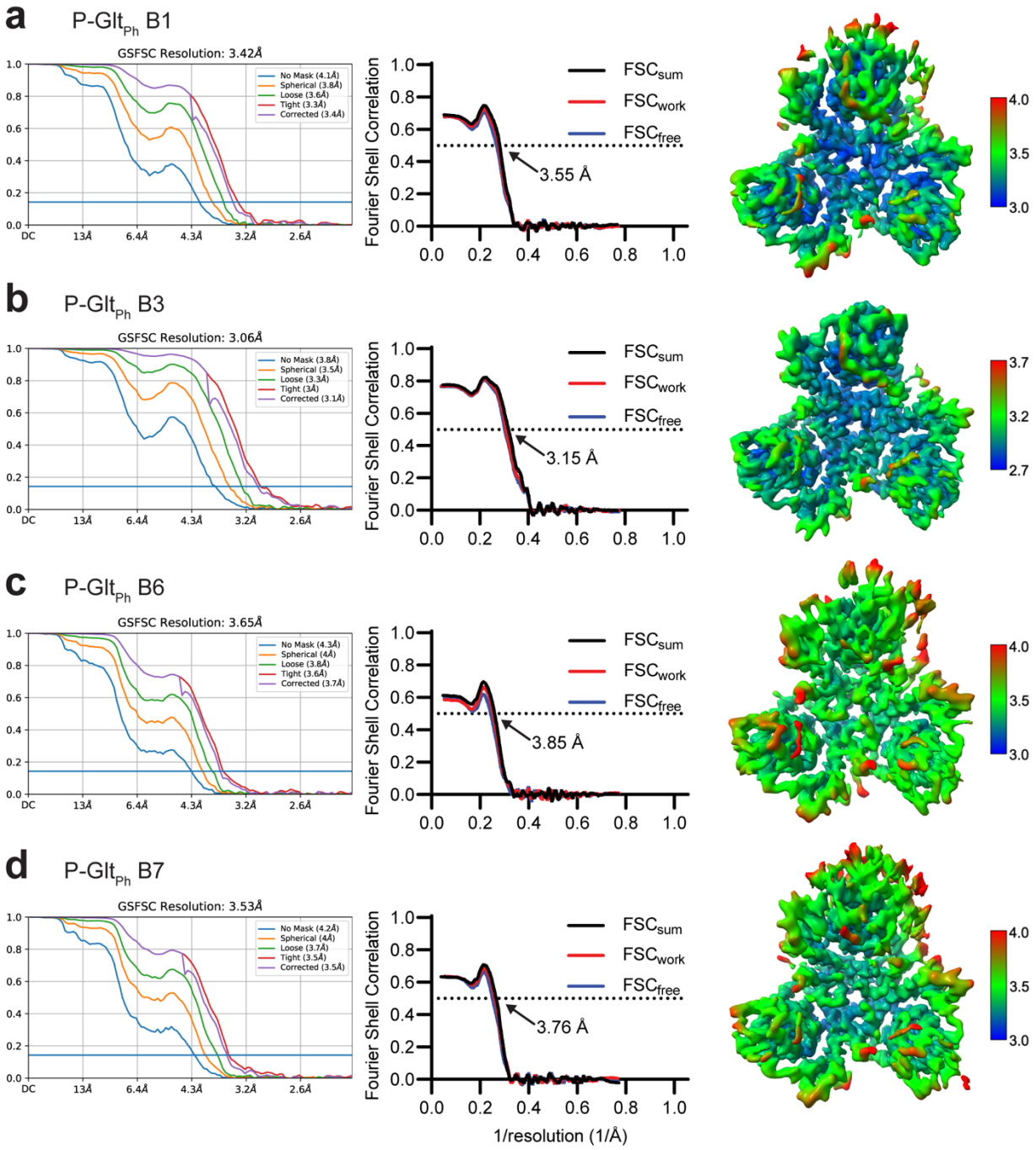

Figure 7 - Supplementary Figure 2. Validation statistics for models from Dataset B. From left to right, map FSC from NU-refinement in cryoSPARC, model-to-data validation in Phenix of the single protomer, and local resolution estimation of the unsharpened map. All structures have a σ of 8. The top protomer is the subject of focused classification and model refinement.

Class	OFS_{out}	OFS_{mid}	OFS_{in}	B1	B3	B6	B7
OFS_{out}		**0.201**	0.234	0.457	0.331	0.571	0.511
OFS_{mid}	0.201		**0.151**	0.434	0.293	0.575	0.485
OFS_{in}	0.234	**0.151**		0.429	0.301	0.577	0.499
B1	0.457	0.434	0.429		**0.389**	0.565	0.506
B3	0.331	**0.293**	0.301	0.389		0.500	0.448
B6	0.571	0.575	0.577	0.565	**0.500**		0.536
B7	0.511	0.485	0.499	0.506	**0.448**	0.536	

Figure 7 – Supplementary Table 2. Comparison between structures from Dataset B and tilt states from Dataset A. Cα RMSDs were determined using 'matchmaker' implemented in ChimeraX using default parameters. Residues 12-106, 130-416 were used for structural alignment to include only well-structured, well-resolved regions. Lowest RMSD values in each row are bolded.

REFERENCES

Adams, P. D., Afonine, P. V., Bunkoczi, G., Chen, V. B., Davis, I. W., Echols, N., . . . Zwart, P. H. (2010). PHENIX: a comprehensive Python-based system for macromolecular structure solution. *Acta Crystallogr D Biol Crystallogr, 66*(Pt 2), 213-221. doi:10.1107/S0907444909052925

Aitken, C. E., Marshall, R. A., & Puglisi, J. D. (2008). An oxygen scavenging system for improvement of dye stability in single-molecule fluorescence experiments. *Biophys J, 94*(5), 1826-1835. doi:10.1529/biophysj.107.117689

Akyuz, N., Altman, R. B., Blanchard, S. C., & Boudker, O. (2013). Transport dynamics in a glutamate transporter homologue. *Nature, 502*(7469), 114-118. doi:10.1038/nature12265

Akyuz, N., Georgieva, E. R., Zhou, Z., Stolzenberg, S., Cuendet, M. A., Khelashvili, G., . . . Blanchard, S. C. (2015). Transport domain unlocking sets the uptake rate of an aspartate transporter. *Nature, 518*(7537), 68-73. doi:10.1038/nature14158

Alleva, C., Kovalev, K., Astashkin, R., Berndt, M. I., Baeken, C., Balandin, T., . . . Machtens, J. P. (2020). Na(+)-dependent gate dynamics and electrostatic attraction ensure substrate coupling in glutamate transporters. *Sci Adv, 6*(47). doi:10.1126/sciadv.aba9854

Arkhipova, V., Guskov, A., & Slotboom, D. J. (2020). Structural ensemble of a glutamate transporter homologue in lipid nanodisc environment. *Nat Commun, 11*(1), 998. doi:10.1038/s41467-020-14834-8

Asarnow, D., Palovcak, E., & Cheng, Y. (2019). *UCSF pyem v0.5*.

Boudker, O., & Oh, S. (2015). Isothermal titration calorimetry of ion-coupled membrane transporters. *Methods, 76*, 171-182. doi:10.1016/j.ymeth.2015.01.012

Boudker, O., Ryan, R. M., Yernool, D., Shimamoto, K., & Gouaux, E. (2007). Coupling substrate and ion binding to extracellular gate of a sodium-dependent aspartate transporter. *Nature, 445*(7126), 387-393. doi:10.1038/nature05455

Brautigam, C. A. (2015). Fitting two- and three-site binding models to isothermal titration calorimetric data. *Methods, 76*, 124-136. doi:10.1016/j.ymeth.2014.11.018

Burguiere, P., Auger, S., Hullo, M. F., Danchin, A., & Martin-Verstraete, I. (2004). Three different systems participate in L-cystine uptake in Bacillus subtilis. *J Bacteriol, 186*(15), 4875-4884. doi:10.1128/JB.186.15.4875-4884.2004

Chakrapani, S., Cordero-Morales, J. F., Jogini, V., Pan, A. C., Cortes, D. M., Roux, B., & Perozo, E. (2011). On the structural basis of modal gating behavior in K(+) channels. *Nat Struct Mol Biol, 18*(1), 67-74. doi:10.1038/nsmb.1968

Chen, V. B., Arendall, W. B., 3rd, Headd, J. J., Keedy, D. A., Immormino, R. M., Kapral, G. J., . . . Richardson, D. C. (2010). MolProbity: all-atom structure validation for macromolecular crystallography. *Acta Crystallogr D Biol Crystallogr, 66*(Pt 1), 12-21. doi:10.1107/S0907444909042073

Ciftci, D., Huysmans, G. H. M., Wang, X., He, C., Terry, D., Zhou, Z., . . . Boudker, O. (2020). Single-molecule transport kinetics of a glutamate transporter homolog shows static disorder. *Sci Adv, 6*(22), eaaz1949. doi:10.1126/sciadv.aaz1949

Colquhoun, D., & Sakmann, B. (1985). Fast events in single-channel currents activated by acetylcholine and its analogues at the frog muscle end-plate. *J Physiol, 369*, 501-557. doi:10.1113/jphysiol.1985.sp015912

Emsley, P., & Cowtan, K. (2004). Coot: model-building tools for molecular graphics. *Acta Crystallogr D Biol Crystallogr, 60*(Pt 12 Pt 1), 2126-2132. doi:10.1107/S0907444904019158

Erkens, G. B., Hanelt, I., Goudsmits, J. M., Slotboom, D. J., & van Oijen, A. M. (2013). Unsynchronised subunit motion in single trimeric sodium-coupled aspartate transporters. *Nature, 502*(7469), 119-123. doi:10.1038/nature12538

Ewers, D., Becher, T., Machtens, J. P., Weyand, I., & Fahlke, C. (2013). Induced fit substrate binding to an archeal glutamate transporter homologue. *Proc Natl Acad Sci U S A, 110*(30), 12486-12491. doi:10.1073/pnas.1300772110

Freidman, N., Chen, I., Wu, Q., Briot, C., Holst, J., Font, J., . . . Ryan, R. (2020). Amino Acid Transporters and Exchangers from the SLC1A Family: Structure, Mechanism and Roles in Physiology and Cancer. *Neurochem Res*. doi:10.1007/s11064-019-02934-x

Freire, E., Schon, A., & Velazquez-Campoy, A. (2009). Isothermal titration calorimetry: general formalism using binding polynomials. *Methods Enzymol, 455*, 127-155. doi:10.1016/S0076-6879(08)04205-5

Gallivan, J. P., & Dougherty, D. A. (1999). Cation-pi interactions in structural biology. *Proc Natl Acad Sci U S A, 96*(17), 9459-9464. doi:10.1073/pnas.96.17.9459

Garaeva, A. A., Guskov, A., Slotboom, D. J., & Paulino, C. (2019). A one-gate elevator mechanism for the human

neutral amino acid transporter ASCT2. *Nat Commun, 10*(1), 3427. doi:10.1038/s41467-019-11363-x

Georgieva, E. R., Borbat, P. P., Ginter, C., Freed, J. H., & Boudker, O. (2013). Conformational ensemble of the sodium-coupled aspartate transporter. *Nat Struct Mol Biol, 20*(2), 215-221. doi:10.1038/nsmb.2494

Grewer, C., Balani, P., Weidenfeller, C., Bartusel, T., Tao, Z., & Rauen, T. (2005). Individual subunits of the glutamate transporter EAAC1 homotrimer function independently of each other. *Biochemistry, 44*(35), 11913-11923. doi:10.1021/bi050987n

Guskov, A., Jensen, S., Faustino, I., Marrink, S. J., & Slotboom, D. J. (2016). Coupled binding mechanism of three sodium ions and aspartate in the glutamate transporter homologue GltTk. *Nat Commun, 7*, 13420. doi:10.1038/ncomms13420

Hall, J. L., Sohail, A., Cabrita, E. J., Macdonald, C., Stockner, T., Sitte, H. H., . . . MacMillan, F. (2020). Saturation transfer difference NMR on the integral trimeric membrane transport protein GltPh determines cooperative substrate binding. *Sci Rep, 10*(1), 16483. doi:10.1038/s41598-020-73443-z

Hanelt, I., Jensen, S., Wunnicke, D., & Slotboom, D. J. (2015). Low Affinity and Slow Na+ Binding Precedes High Affinity Aspartate Binding in the Secondary-active Transporter GltPh. *J Biol Chem, 290*(26), 15962-15972. doi:10.1074/jbc.M115.656876

Hanelt, I., Wunnicke, D., Bordignon, E., Steinhoff, H. J., & Slotboom, D. J. (2013). Conformational heterogeneity of the aspartate transporter Glt(Ph). *Nat Struct Mol Biol, 20*(2), 210-214. doi:10.1038/nsmb.2471

Huang, Y., Wang, X., Lv, G., Razavi, A. M., Huysmans, G. H. M., Weinstein, H., . . . Boudker, O. (2020). Use of paramagnetic (19)F NMR to monitor domain movement in a glutamate transporter homolog. *Nat Chem Biol*. doi:10.1038/s41589-020-0561-6

Huysmans, G. H. M., Ciftci, D., Wang, X., Blanchard, S. C., & Boudker, O. (2021). The high-energy transition state of the glutamate transporter homologue GltPh. *EMBO J, 40*(1), e105415. doi:10.15252/embj.2020105415

Juette, M. F., Terry, D. S., Wasserman, M. R., Altman, R. B., Zhou, Z., Zhao, H., & Blanchard, S. C. (2016). Single-molecule imaging of non-equilibrium molecular ensembles on the millisecond timescale. *Nat Methods, 13*(4), 341-344. doi:10.1038/nmeth.3769

Kim, Y. M., Ogawa, W., Tamai, E., Kuroda, T., Mizushima, T., & Tsuchiya, T. (2002). Purification, reconstitution, and characterization of Na(+)/serine symporter, SstT, of Escherichia coli. *J Biochem, 132*(1), 71-76. doi:10.1093/oxfordjournals.jbchem.a003201

Koch, H. P., Brown, R. L., & Larsson, H. P. (2007). The glutamate-activated anion conductance in excitatory amino acid transporters is gated independently by the individual subunits. *J Neurosci, 27*(11), 2943-2947. doi:10.1523/JNEUROSCI.0118-07.2007

Koch, H. P., & Larsson, H. P. (2005). Small-scale molecular motions accomplish glutamate uptake in human glutamate transporters. *J Neurosci, 25*(7), 1730-1736. doi:10.1523/JNEUROSCI.4138-04.2005

Le, V. H., Buscaglia, R., Chaires, J. B., & Lewis, E. A. (2013). Modeling complex equilibria in isothermal titration calorimetry experiments: thermodynamic parameters estimation for a three-binding-site model. *Anal Biochem, 434*(2), 233-241. doi:10.1016/j.ab.2012.11.030

Livnat-Levanon, N., A, I. G., Ben-Tal, N., & Lewinson, O. (2016). The uncoupled ATPase activity of the ABC transporter BtuC2D2 leads to a hysteretic conformational change, conformational memory, and improved activity. *Sci Rep, 6*, 21696. doi:10.1038/srep21696

Mastronarde, D. N. (2005). Automated electron microscope tomography using robust prediction of specimen movements. *J Struct Biol, 152*(1), 36-51. doi:10.1016/j.jsb.2005.07.007

Matin, T. R., Heath, G. R., Huysmans, G. H. M., Boudker, O., & Scheuring, S. (2020). Millisecond dynamics of an unlabeled amino acid transporter. *Nature Communications, 11*(1), 5016. doi:10.1038/s41467-020-18811-z

McIlwain, B. C., Vandenberg, R. J., & Ryan, R. M. (2016). Characterization of the Inward- and Outward-Facing Substrate Binding Sites of the Prokaryotic Aspartate Transporter, GltPh. *Biochemistry, 55*(49), 6801-6810. doi:10.1021/acs.biochem.6b00795

Meng, E. C., Pettersen, E. F., Couch, G. S., Huang, C. C., & Ferrin, T. E. (2006). Tools for integrated sequence-structure analysis with UCSF Chimera. *BMC Bioinformatics, 7*, 339. doi:10.1186/1471-2105-7-339

Oh, S., & Boudker, O. (2018). Kinetic mechanism of coupled binding in sodium-aspartate symporter GltPh. *Elife, 7*. doi:10.7554/eLife.37291

Pettersen, E. F., Goddard, T. D., Huang, C. C., Couch, G. S., Greenblatt, D. M., Meng, E. C., & Ferrin, T. E. (2004). UCSF Chimera--a visualization system for exploratory research and analysis. *J Comput Chem, 25*(13), 1605-1612. doi:10.1002/jcc.20084

Pettersen, E. F., Goddard, T. D., Huang, C. C., Meng, E. C., Couch, G. S., Croll, T. I., . . . Ferrin, T. E. (2021).

UCSF ChimeraX: Structure visualization for researchers, educators, and developers. *Protein Sci, 30*(1), 70-82. doi:10.1002/pro.3943

Popescu, G. K. (2012). Modes of glutamate receptor gating. *J Physiol, 590*(1), 73-91. doi:10.1113/jphysiol.2011.223750

Punjani, A., & Fleet, D. J. (2021). 3D variability analysis: Resolving continuous flexibility and discrete heterogeneity from single particle cryo-EM. *J Struct Biol, 213*(2), 107702. doi:10.1016/j.jsb.2021.107702

Punjani, A., Rubinstein, J. L., Fleet, D. J., & Brubaker, M. A. (2017). cryoSPARC: algorithms for rapid unsupervised cryo-EM structure determination. *Nat Methods, 14*(3), 290-296. doi:10.1038/nmeth.4169

Punjani, A., Zhang, H., & Fleet, D. J. (2020). Non-uniform refinement: adaptive regularization improves single-particle cryo-EM reconstruction. *Nat Methods, 17*(12), 1214-1221. doi:10.1038/s41592-020-00990-8

Qiu, B., Matthies, D., Fortea, E., Yu, Z., & Boudker, O. (2020). Transport mechanism of the neuronal excitatory amino acid transporter. *bioRxiv*, 2020.2006.2001.127704. doi:10.1101/2020.06.01.127704

Reyes, N., Ginter, C., & Boudker, O. (2009). Transport mechanism of a bacterial homologue of glutamate transporters. *Nature, 462*(7275), 880-885. doi:10.1038/nature08616

Reyes, N., Oh, S., & Boudker, O. (2013). Binding thermodynamics of a glutamate transporter homolog. *Nat Struct Mol Biol, 20*(5), 634-640. doi:10.1038/nsmb.2548

Riederer, E. A., Focke, P. J., Georgieva, E. R., Akyuz, N., Matulef, K., Borbat, P. P., . . . Valiyaveetil, F. I. (2018). A facile approach for the in vitro assembly of multimeric membrane transport proteins. *Elife, 7*. doi:10.7554/eLife.36478

Riederer, E. A., & Valiyaveetil, F. I. (2019). Investigation of the allosteric coupling mechanism in a glutamate transporter homolog via unnatural amino acid mutagenesis. *Proc Natl Acad Sci U S A, 116*(32), 15939-15946. doi:10.1073/pnas.1907852116

Rohou, A., & Grigorieff, N. (2015). CTFFIND4: Fast and accurate defocus estimation from electron micrographs. *J Struct Biol, 192*(2), 216-221. doi:10.1016/j.jsb.2015.08.008

Ruan, Y., Miyagi, A., Wang, X., Chami, M., Boudker, O., & Scheuring, S. (2017). Direct visualization of glutamate transporter elevator mechanism by high-speed AFM. *Proc Natl Acad Sci U S A, 114*(7), 1584-1588. doi:10.1073/pnas.1616413114

Ryan, R. M., Compton, E. L., & Mindell, J. A. (2009). Functional characterization of a Na+-dependent aspartate transporter from Pyrococcus horikoshii. *J Biol Chem, 284*(26), 17540-17548. doi:10.1074/jbc.M109.005926

Ryan, R. M., & Mindell, J. A. (2007). The uncoupled chloride conductance of a bacterial glutamate transporter homolog. *Nat Struct Mol Biol, 14*(5), 365-371. doi:10.1038/nsmb1230

Scheres, S. H. (2016). Processing of Structurally Heterogeneous Cryo-EM Data in RELION. *Methods Enzymol, 579*, 125-157. doi:10.1016/bs.mie.2016.04.012

Su, M., Zhu, L., Zhang, Y., Paknejad, N., Dey, R., Huang, J., . . . Huang, X. Y. (2020). Structural Basis of the Activation of Heterotrimeric Gs-Protein by Isoproterenol-Bound beta1-Adrenergic Receptor. *Mol Cell, 80*(1), 59-71 e54. doi:10.1016/j.molcel.2020.08.001

Suloway, C., Pulokas, J., Fellmann, D., Cheng, A., Guerra, F., Quispe, J., . . . Carragher, B. (2005). Automated molecular microscopy: the new Leginon system. *J Struct Biol, 151*(1), 41-60. doi:10.1016/j.jsb.2005.03.010

Terwilliger, T. C., Ludtke, S. J., Read, R. J., Adams, P. D., & Afonine, P. V. (2020). Improvement of cryo-EM maps by density modification. *Nat Methods, 17*(9), 923-927. doi:10.1038/s41592-020-0914-9

Verdon, G., & Boudker, O. (2012). Crystal structure of an asymmetric trimer of a bacterial glutamate transporter homolog. *Nat Struct Mol Biol, 19*(3), 355-357. doi:10.1038/nsmb.2233

Verdon, G., Oh, S., Serio, R. N., & Boudker, O. (2014). Coupled ion binding and structural transitions along the transport cycle of glutamate transporters. *Elife, 3*, e02283. doi:10.7554/eLife.02283

Veshaguri, S., Christensen, S. M., Kemmer, G. C., Ghale, G., Moller, M. P., Lohr, C., . . . Stamou, D. (2016). Direct observation of proton pumping by a eukaryotic P-type ATPase. *Science, 351*(6280), 1469-1473. doi:10.1126/science.aad6429

Wang, J., Li, P., Yu, X., & Grewer, C. (2021). Observing spontaneous, accelerated substrate binding in molecular dynamics simulations of glutamate transporters. *PLoS One, 16*(4), e0250635. doi:10.1371/journal.pone.0250635

Wang, X., & Boudker, O. (2020). Large domain movements through the lipid bilayer mediate substrate release and inhibition of glutamate transporters. *Elife, 9*. doi:10.7554/eLife.58417

Yernool, D., Boudker, O., Jin, Y., & Gouaux, E. (2004). Structure of a glutamate transporter homologue from Pyrococcus horikoshii. *Nature, 431*(7010), 811-818. doi:10.1038/nature03018

Youn, J. W., Jolkver, E., Kramer, R., Marin, K., & Wendisch, V. F. (2009). Characterization of the dicarboxylate transporter DctA in Corynebacterium glutamicum. *J Bacteriol, 191*(17), 5480-5488. doi:10.1128/JB.00640-09

Zerangue, N., & Kavanaugh, M. P. (1996). Flux coupling in a neuronal glutamate transporter. *Nature, 383*(6601), 634-637. doi:10.1038/383634a0

Zhang, Y., & Cremer, P. S. (2006). Interactions between macromolecules and ions: The Hofmeister series. *Curr Opin Chem Biol, 10*(6), 658-663. doi:10.1016/j.cbpa.2006.09.020

Zheng, S. Q., Palovcak, E., Armache, J. P., Verba, K. A., Cheng, Y., & Agard, D. A. (2017). MotionCor2: anisotropic correction of beam-induced motion for improved cryo-electron microscopy. *Nat Methods, 14*(4), 331-332. doi:10.1038/nmeth.4193

Zivanov, J., Nakane, T., Forsberg, B. O., Kimanius, D., Hagen, W. J., Lindahl, E., & Scheres, S. H. (2018). New tools for automated high-resolution cryo-EM structure determination in RELION-3. *Elife, 7*. doi:10.7554/eLife.42166